Modelling the mercury stable isotope distribution of Earth surface reservoirs: Implications for global Hg cycling

Ruoyu Sun [a,*], Martin Jiskra [b], Helen M. Amos [c], Yanxu Zhang [d]
Elsie M. Sunderland [c,e], Jeroen E. Sonke [b,*]

[a] *Institute of Surface-Earth System Science, Tianjin University, Tianjin 300072, China*
[b] *Observatoire Midi-Pyrénées, Laboratoire Géosciences Environnement Toulouse, CNRS/IRD/Université Paul Sabatier, Toulouse 3, France*
[c] *School of Public Health, Department of Environmental Health, Harvard University, Boston, MA, USA*
[d] *School of Atmospheric Sciences, Nanjing University, Jiangsu 210023, China*
[e] *School of Engineering and Applied Sciences, Harvard University, Cambridge, MA, USA*

Abstract

Mercury (Hg) stable isotopes are useful to understand Hg biogeochemical cycling because physical, chemical and biological processes cause characteristic Hg isotope mass-dependent (MDF) and mass-independent (MIF) fractionation. Here, source Hg isotope signatures and process-based isotope fractionation factors are integrated into a fully coupled, global atmospheric-terrestrial-oceanic box model of MDF ($\delta^{202}Hg$), odd-MIF ($\Delta^{199}Hg$) and even-MIF ($\Delta^{200}Hg$). Using this bottom-up approach, we find that the simulated Hg isotope compositions are inconsistent with the observations. We then fit the Hg isotope enrichment factors for MDF, odd-MIF and even-MIF to observational Hg isotope constraints. The MDF model suggests that atmospheric Hg^0 photo-oxidation should enrich heavy Hg isotopes in the reactant Hg^0, in contrast to the experimental observations of Hg^0 photo-oxidation by Br. The fitted enrichment factor of terrestrial Hg^0 emission in the odd-MIF model (5‰) is likely biased high, suggesting that the terrestrial Hg^0 emission flux (160 Mg yr^{-1}) used in our standard model is underestimated. In the even-MIF model, we find that a small positive atmospheric Hg^0 photo-oxidation enrichment factor (0.22‰) along with enhanced atmospheric Hg^{II} photo-reduction and atmospheric Hg^0 dry deposition (foliar uptake) fluxes to the terrestrial reservoir are needed to match $\Delta^{200}Hg$ observations. Marine Hg isotope measurements are needed to further expand the use of Hg isotopes in understanding global Hg cycling.
© 2018 Elsevier Ltd. All rights reserved.

Keywords: Mercury isotope; Global Hg cycling; Box model; Mass-dependent fractionation; Mass-independent fractionation

1. INTRODUCTION

Mercury (Hg) is a globally distributed toxic element. Both geogenic processes and human activities liberate Hg from Earth's lithosphere into the surface environment. Geogenic Hg is mainly released into the atmosphere in forms of volcanic and hydrothermal degassing (Pyle and Mather, 2003; Bagnato et al., 2014). From ∼3000 BCE, humans started to increase Hg releases by silver/gold mining, fossil fuel combustion and non-ferrous metal smelting (Nriagu, 1979; Streets et al., 2011). Following releases, Hg cycles among atmospheric, terrestrial and oceanic reservoirs before ultimately being buried in marine sediments and returning to the lithosphere (Andren and Nriagu, 1979; Mason et al., 1994; Amos et al., 2014). Understanding the natural and anthropogenic Hg cycles is critical to quantify

---

the amounts of legacy Hg accumulated at the Earth's surface, and to predict how Hg emission reduction policies (e.g., Mercury Minimata Convention) will affect Hg budgets in biogeochemical reservoirs (Amos et al., 2013, 2014). However, large uncertainties still exist for the global Hg cycle regarding the magnitude of numerous fluxes and transformations including atmospheric Hg^0 oxidation and Hg^{II} reduction, Hg dry/wet deposition, and marine-atmospheric and terrestrial-atmospheric Hg^0 exchange (Lindberg et al., 2007; Pongprueksa et al., 2008; Holmes et al., 2010; Streets et al., 2011; Engstrom et al., 2014; Obrist et al., 2014; Huang and Gustin, 2015; Agnan et al., 2016).

Mercury stable isotopes are a new tool to study Hg cycling at various spatiotemporal scales (Sonke, 2011; Hintelmann, 2012; Sonke and Blum, 2013; Blum et al., 2014; Yin et al., 2014). The seven Hg stable isotopes can be fractionated mass-dependently (MDF, indicated by $\delta^{202}Hg$) and mass-independently (odd-MIF for odd mass number Hg isotopes indicated by $\Delta^{199}Hg$ or $\Delta^{201}Hg$, and even-MIF for even mass number Hg isotopes indicated by $\Delta^{200}Hg$ or $\Delta^{204}Hg$). MDF occurs during nearly all abiotic and biotic Hg transformations, and causes the separation between heavy and light Hg isotopes due to the differences in their nuclear masses and volumes (Blum et al., 2014; Yin et al., 2014). Odd-MIF occurs in specific processes that are selective to nuclear spin or nuclear volume, and causes the separation between even and odd mass number Hg isotopes due to the non-zero nuclear spins (magnetic isotope effect, MIE) (Buchachenko, 2001, 2009; Bergquist and Blum, 2007) or the nuclear size/shape distortion of odd mass number Hg isotopes (nuclear volume effect, NVE) (Schauble, 2007; Zheng and Hintelmann, 2010b; Ghosh et al., 2013). More than 10‰ variation in both MDF and odd-MIF are reported across the Earth's reservoirs (Blum et al., 2014; Yin et al., 2014). Even-MIF is mainly observed in the atmosphere with more than 1‰ variation, but the underlying mechanisms are still unclear (Chen et al., 2012; Cai and Chen, 2015).

Physical, chemical and biological processes drive Hg mass transfer from one reservoir to another, and each process fractionates heavy/light and odd/even Hg isotopes along characteristic trajectories (Blum et al., 2014). The Hg mass transfer and Hg isotope fractionation processes result in biogeochemical reservoirs with distinct Hg isotope signatures. For example, the contrasting $\delta^{202}Hg$, $\Delta^{199}Hg$, and $\Delta^{200}Hg$ signatures of atmospheric Hg^0 and Hg^{II} lead to powerful applications in tracing Hg^{II} wet and Hg^0 dry deposition pathways (Demers et al., 2013; Enrico et al., 2016; Obrist et al., 2017). Across the Arctic tundra, and the North American and European boreal and temperate forested ecosystems, Hg isotope signatures in soils show that Hg deposited through plant uptake of atmospheric Hg^0 exceeds Hg originating from atmospheric Hg^{II} wet deposition by a factor 2–4 (Demers et al., 2013; Jiskra et al., 2015; Enrico et al., 2016; Zheng et al., 2016; Obrist et al., 2017). We have only yet begun to understand the consequences of such a paradigm shift. Enrico et al. (2016) argued that plant uptake lowers atmospheric Hg^0 lifetime to 4 months. Enrico et al. (2017) used a peat archive to reconstruct the first millennial record of plant Hg^0 uptake, and found Holocene Hg^0 levels to be more than 10 times lower than maximum 20th century Hg^0. Obrist et al. (2017) showed how tundra uptake of Hg^0 has loaded tundra soils with vast amounts of Hg, that risk being mobilized into the Arctic Ocean by rivers as permafrost soils thaw. We are therefore at a turning point in Hg isotope science, where isotope signatures provide strong constraints and insights on some of the lesser known Hg fluxes and processes at the Earth's surface.

Here we construct a global Hg isotope box model on the basis of the state-of-the-science global Hg chemistry and transport models (Amos et al., 2014; Zhang et al., 2015) where Hg sources and Hg mass transfer processes are complemented with Hg isotope signatures. The initial aim of this Hg isotope model is to examine if Hg isotope observations in atmospheric, terrestrial and oceanic reservoirs can be reproduced using current knowledge on the global Hg cycle, source Hg isotope signatures and Hg isotope fractionation processes. We then investigate how the observed Hg isotope compositions in the Earth's reservoirs can be used to further constrain global Hg mass transfer processes.

2. METHODS

2.1. Hg isotope notations

The Hg isotope composition is expressed in delta notation (δ, ‰) by anchoring to a common NIST SRM 3133 Hg standard:

$$\delta^{xxx}Hg(‰) = \left[\left(^{xxx}Hg/^{198}Hg\right)_{sample} / \left(^{xxx}Hg/^{198}Hg\right)_{NIST3133} - 1\right] \times 1000 \tag{1}$$

where the superscript XXX is Hg isotope mass number between 199 and 204, $(^{XXX}Hg/^{198}Hg)$sample is isotope ratio of the sample, and $(^{XXX}Hg/^{198}Hg)$NIST 3133 is the isotope ratio of the bracketing NIST SRM 3133 Hg standard. The Hg isotope MIF is expressed in capital delta notation (Δ, ‰), representing the difference between the measured $\delta^{xxx}Hg$ and that predicted from $\delta^{202}Hg$ using a kinetic MDF law (Blum and Bergquist, 2007):

$$\Delta^{xxx}Hg(‰) = \delta^{xxx}Hg - {}^{xxx}\beta \times \delta^{202}Hg \tag{2}$$

The mass dependent scaling factor $^{xxx}\beta$ is 0.2520 for ^{199}Hg, 0.5024 for ^{200}Hg, 0.7520 for ^{201}Hg and 1.4930 for ^{204}Hg. In this study, we use $\delta^{202}Hg$, $\Delta^{199}Hg$ and $\Delta^{200}Hg$ as the tracers of MDF, odd-MIF and even-MIF, respectively.

The total Hg isotope fractionation factor (α) between reactant i (reservoir i) and product j (reservoir j) is defined as:

$$\alpha^{xxx}Hg_{TOT(i \to j)} = \frac{R^{xxx}Hg_j}{R^{xxx}Hg_i} = \frac{(^{xxx}Hg/^{198}Hg)_j}{(^{xxx}Hg/^{198}Hg)_i} \tag{3}$$

and can be decomposed into MDF, odd-MIF and even-MIF components (Sonke, 2011):

$$\alpha^{xxx}Hg_{TOT(i\to j)} = \alpha^{xxx}Hg_{MDF(i\to j)} \times \alpha^{xxx}Hg_{odd-MIF(i\to j)}$$
$$\times \alpha^{xxx}Hg_{even-MIF(i\to j)} \quad (4)$$

Both $\alpha^{202}Hg_{odd\text{-}MIF}$ and $\alpha^{202}Hg_{even\text{-}MIF}$ equal to 1 for $\alpha^{202}Hg_{TOT}$; $\alpha^{199}Hg_{even\text{-}MIF}$ equals to 1 for $\alpha^{199}Hg_{TOT}$; $\alpha^{200}Hg_{odd\text{-}MIF}$ equals to 1 for $\alpha^{200}Hg_{TOT}$. The Hg isotope enrichment factor expressed in epsilon notation (ε or E) is used to denote 'permil fractionation factor', which we use from here on:

$$\varepsilon^{202}Hg(\text{‰}) = 1000 \times (\alpha^{202}Hg_{MDF} - 1);$$
$$E^{199}Hg(\text{‰}) = 1000 \times (\alpha^{199}Hg_{odd-MIF} - 1);$$
$$E^{200}Hg(\text{‰}) = 1000 \times (\alpha^{200}Hg_{even-MIF} - 1) \quad (5)$$

2.2. Model description

The basic structure of the global Hg isotope box model is based on the 7-box model of Amos et al. (2013, 2014) that is used to simulate global biogeochemical cycle of total Hg (THg). Here, we further separate the atmospheric THg box into gaseous elemental Hg^0 and oxidized Hg^{II} (including gaseous oxidized Hg^{II} and particulate-bound Hg^P) based on the GEOS-Chem model of Holmes et al. (2010). THg in the surface, intermediate and deep ocean layers is also speciated as dissolved Hg^0, dissolved Hg^{II} and particulate-bound Hg^P based on a global 3D ocean general circulation model (MITgcm) (Zhang et al., 2015). Thus, the global Hg isotope box model comprises 14 Hg reservoirs (named as Global 14-Box Model of Hg Isotopes, user instruction and model codes are available at https://github.com/ruoyusun/GBM-Hg-ISO-14box-v1.git): atmospheric $\mathbf{Hg_{atm}^0}$, atmospheric $\mathbf{Hg_{atm}^{II}}$, fast terrestrial $\mathbf{Hg_{tf}}$, slow terrestrial $\mathbf{Hg_{ts}}$, armored terrestrial $\mathbf{Hg_{ta}}$, surface oceanic $\mathbf{Hg_{ocs}^0}$, surface oceanic $\mathbf{Hg_{ocs}^{II}}$, surface oceanic $\mathbf{Hg_{ocs}^P}$, intermediate oceanic $\mathbf{Hg_{oci}^0}$, intermediate oceanic $\mathbf{Hg_{oci}^{II}}$, intermediate oceanic $\mathbf{Hg_{oci}^P}$, deep oceanic $\mathbf{Hg_{ocd}^0}$, deep oceanic $\mathbf{Hg_{ocd}^{II}}$, and deep oceanic $\mathbf{Hg_{ocd}^P}$ (Fig. 1). Organic Hg species (e.g. monomethylmercury and dimethylmercury) are not included in the model at this stage and are implicitly included in THg.

Mass transfer of Hg between boxes are controlled by first-order time-invariant rate coefficients (k, yr^{-1}), and are represented by a group of 14 coupled ordinary differential equations (ODEs):

$$\frac{dM_i}{dt} = \sum_{j\neq i}(k_{j\to i} \times M_j) - \sum_{i\neq j}(k_{i\to j} \times M_i) + S \quad (6)$$

where M_i (Mg) is the Hg mass in box 'i', and M_j (Mg) is the Hg mass in box 'j'. $k_{j\to i} = F_{j\to i}/M_j$ and $k_{i\to j} = F_{i\to j}/M_i$ are the first-order rate coefficients, in which $F_{j\to i}$ (Mg yr^{-1}) is Hg flux from box 'j' to box 'i' and $F_{i\to j}$ (Mg yr^{-1}) is Hg flux from box 'i' to box 'j'. S (Mg yr^{-1}) is external Hg input from the deep mineral reservoir by natural and/or anthropogenic processes (0 for all reservoirs except for the atmosphere and surfaceocean). Sequestration of riverine Hg^P in coastal margin sediments and Hg^P in deep oceanic sediments are treated as permanent Hg removal processes.

Fractionation of Hg isotopes between boxes are controlled by time-invariant Hg isotope enrichment factors

(ε or E), and are also represented as a group of 14 coupled ODEs:

$$\frac{d(M_i \times \delta^{202}Hg_i)}{dt} = \sum_{j\neq i}\left[k_{j\to i} \times M_j \times \left(\delta^{202}Hg_j + \varepsilon^{202}Hg_{(j\to i)}\right)\right]$$
$$- \sum_{i\neq j}\left[k_{i\to j} \times M_i \times \left(\delta^{202}Hg_i + \varepsilon^{202}Hg_{(i\to j)}\right)\right]$$
$$+ S \times \delta^{202}Hg_S \quad (7)$$

for MDF, or

$$\frac{d(M_i \times \Delta^{xxx}Hg_i)}{dt} = \sum_{j\neq i}\left[k_{j\to i} \times M_j \times \left(\Delta^{xxx}Hg_j + E^{xxx}Hg_{(j\to i)}\right)\right]$$
$$- \sum_{i\neq j}\left[k_{i\to j} \times M_i \times \left(\Delta^{xxx}Hg_i + E^{xxx}Hg_{(i\to j)}\right)\right]$$
$$+ S \times \Delta^{xxx}Hg_S \quad (8)$$

for odd-MIF ($\Delta^{199}Hg$) or even-MIF ($\Delta^{200}Hg$). Since Hg redox transformations are one-way kinetic processes, the MDF and MIF isotope enrichment factors represent kinetic isotope fractionation. The time-step (dt) of the ODE solver algorithm is small enough to avoid Rayleigh-type reservoir effects.

From the Eqs. (6)–(8), the global Hg isotope model comprises four basic components: rate coefficient k, geogenic/anthropogenic Hg input inventory S and its isotope composition $\delta^{202}Hg_S$ or $\Delta^{xxx}Hg_S$, and Hg isotope enrichment factor ε or E. The rate coefficients are calculated from present-day reservoir Hg sizes and Hg fluxes between reservoirs, based on the GEOS-Chem and MITgcm models (summarized in Table EA-1 and explained in the Electronic Annex). We use the same Hg input inventory as Amos et al. (2014), which includes geogenic (90 Mg/yr) (Bagnato et al., 2011) and anthropogenic (2000 BCE to 2010 CE, cumulatively 460,000 Mg) Hg emissions into the atmosphere (Streets et al., 2011; Horowitz et al., 2014) and anthropogenic Hg discharges into the river (1850 CE–2010 CE, cumulatively 380,000 Mg) (Amos et al., 2014). The riverine Hg is then delivered to the surface ocean after partial burial in coastal margin sediments (Amos et al., 2014). Previous studies have evaluated the uncertainties of these Hg input inventories (Streets et al., 2011; Amos et al., 2014; Horowitz et al., 2014), and demonstrated that their use in the Hg cycling models could result in output compatible with observed Earth's budgets and fluxes (Amos et al., 2013, 2014, 2015). The isotope composition of Hg input inventory and Hg isotope enrichment factor are discussed below.

2.2.1. Isotope composition of Hg input inventory

The geogenic Hg emissions are derived from observations on volcanic plumes as summarized by Bagnato et al. (2011). Volcanic fumarole plume THg has a mean value of -0.76‰ $\pm$ 0.11‰ (1σ) for $\delta^{202}Hg$ and of 0.05‰ $\pm$ 0.03‰ (1σ) for $\Delta^{199}Hg$ (Zambardi et al., 2009; Sun et al., 2016b). Thus, the geogenic Hg emissions are assumed to have a $\delta^{202}Hg$ value of -0.76‰ $\pm$ 0.11‰ (1σ). The anthropogenic Hg emissions to the atmosphere are separated as gaseous Hg^0, gaseous Hg^{II} and particulate-bound Hg^P,
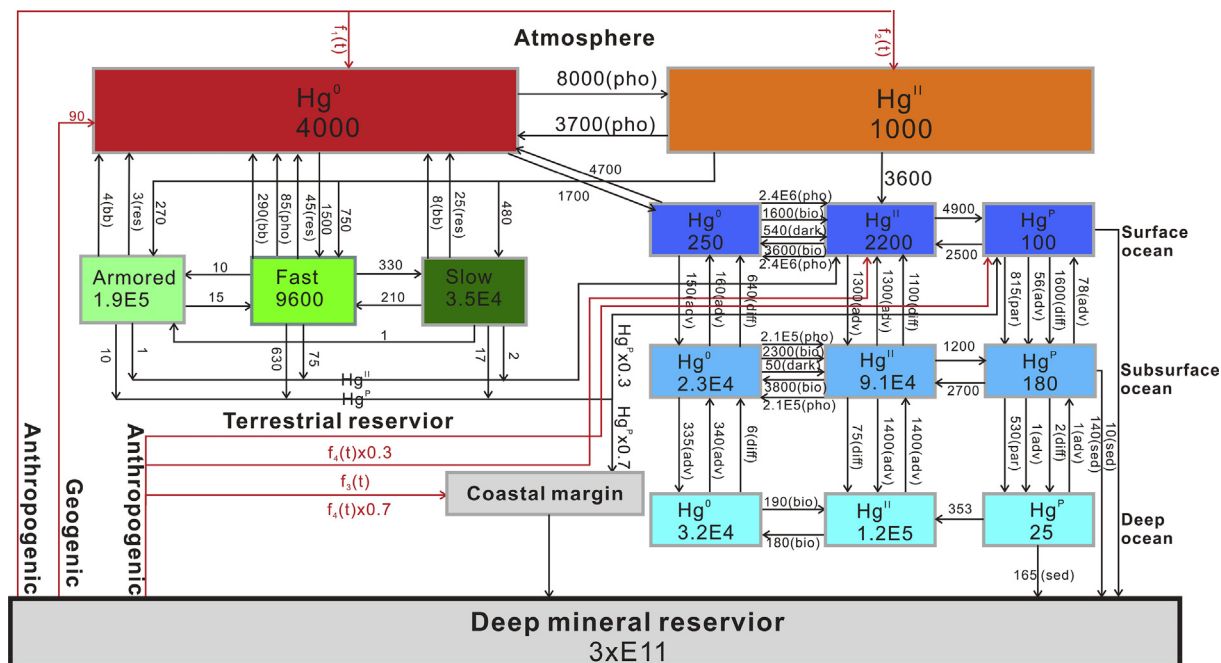
Fig. 1. The basic structure of global Hg isotope box model where the numbers in boxes represent the each Hg reservoir size (Mg), the numbers beside the black arrows represent Hg mass transfer fluxes (Mg yr^{-1}), and the numbers and functions besides the red arrows represent the geogenic and anthropogenic input Hg fluxes (Mg yr^{-1}) in modern days. The multiple Hg mass transfer fluxes from one box to another are differentiated by arrows with processes identifiers (pho: photochemical; bio: biotic; bb: biomass burning; res: respiration; adv: advection; diff: diffusion; sed: sedimentation; par: particle-setting). See Table A1 in the electronic annex for details.

and their Hg isotope compositions and associated uncertainties between 1850 and 2010 were estimated by Sun et al. (2016b) after correcting the isotope shifts during processing and combustion of anthropogenic source materials. Pre-1850 Hg emissions mostly originated from the intentional liquid Hg^0 use in silver production (58%) and Hg ore mining (30%) around the 16th–18th centuries in South/Central America (Streets et al., 2011). We assume these emissions to be near-quantitative and in the gaseous Hg^0 form, and should therefore conserve the Hg isotope signatures of source materials. According to anthropogenic Hg emission budgets of individual sectors before 1850 and their source material Hg isotope compositions, we estimate a median value of −0.91‰ (−1.49‰ to −0.49‰ at 80% confidence level) for δ^{202}Hg and of 0.00‰ (−0.04‰ to 0.04‰ at 80% confidence level) for Δ^{199}Hg, following Sun et al. (2016b). Since modern rivers mainly receive effluent Hg from industrial sectors that intentionally use liquid Hg^0 (Amos et al., 2014; Horowitz et al., 2014; Wiederhold et al., 2015), the direct anthropogenic Hg discharges into rivers are assumed to have the Hg isotope composition of commercial liquid Hg^0 (δ^{202}Hg = −0.49‰ ± 0.40‰, Δ^{199}Hg = −0.01‰ ± 0.05‰, 1σ) (Blum and Bergquist, 2007; Sonke et al., 2008; Estrade et al., 2009; Foucher et al., 2009; Laffont et al., 2011; Gray et al., 2013; Mead et al., 2013; Ruaibarz et al., 2016). As geogenic emissions and riverine discharges have very small Δ^{199}Hg values, within the typical measurement uncertainty (±0.05‰ to ±0.10‰), we assume that they have no odd-MIF anomalies (i.e. Δ^{199}Hg = 0.00‰). Following Sun

et al. (2016b), we assume that geogenic and anthropogenic Hg sources have no even-MIF anomalies (i.e. Δ^{200}Hg = 0.00‰).

2.2.2. Isotope enrichment factor

The Hg isotope enrichment factors in the model are derived from laboratory-controlled experiments where possible, or empirically estimated from the literature, or unknown. Table EA-2 lists the experimental enrichment factors for MDF (ε^{202}Hg) and odd-MIF (E^{199}Hg) during physical, chemical and biological transformation of inorganic Hg. We note that these enrichment factors were obtained under controlled laboratory conditions and their extrapolation to the natural environment is associated with large uncertainties. In the following, we discuss the experimental conditions under which enrichment factors were determined and the rationale for the selection of specific literature values for the MDF and odd-MIF 'standard model' simulation in Tables 1 and 2. A small amount of even-MIF (E^{200}Hg$_{atm\ (0-II)}$ = 0.06‰ ± 0.01‰, 1σ) was only observed in the photochemical reaction of Hg^0 + Br/Cl (Sun et al., 2016a). Thus, we use a value of 0.05‰ for E^{200}Hg$_{atm\ (0-II)}$ in even-MIF 'standard model' simulation (Table 3).

2.2.2.1. Oxidation of gaseous Hg^0.
Gaseous Hg^0 photo-oxidation experiments under normal atmospheric condition (25 °C, 750 Torr) showed that the reaction of Hg^0 + Br induced both MDF and odd-MIF. The reactant Hg^0 became progressively enriched in the light (ε^{202}Hg = 0.74‰ ± 0.07, 1σ) and odd Hg isotopes

Table 1
Observed and simulated $\delta^{202}Hg$ (‰) in the Earth's reservoirs by standard and fitted MDF box models (the fitted enrichment factors are shown in bold).

Enrichment factor (‰)	Observed mean ± 1SD	Model simulation	
		Standard	#1
$\varepsilon^{202}Hg_{atm\ (0-II)}$ (atmospheric Hg^0 oxidation, photo-)		0.75	**−0.85**
$\varepsilon^{202}Hg_{ocean\ (0-II)}$ (marine Hg^0 oxidation, photo-)		0.00	0.00
$\varepsilon^{202}Hg_{atm\ (II-0)}$ (atmospheric Hg^{II} reduction, photo-)		−0.80	−0.80
$\varepsilon^{202}Hg_{ocean\ (II-0)}$ (marine Hg^{II} reduction, photo-)		−0.80	−0.80
$\varepsilon^{202}Hg_{ocean\ (II-0)}$ (marine Hg^{II} reduction, biotic-)		−0.40	−0.40
$\varepsilon^{202}Hg_{ocean\ (II-P)}$ (marine Hg^{II} partition to Hg^P)		−0.50	−0.50
$\varepsilon^{202}Hg_{ter\ (II-0)}$ (terrestrial Hg^0 emission, photo-)		−1.30	−1.30
$\varepsilon^{202}Hg_{ter\ (II-0)}$ (terrestrial Hg^0 emission, nonphoto-)		−1.50	−1.50
$\varepsilon^{202}Hg_{atm-ter\ (0-II)}$ (atmospheric Hg^0 deposition, foliar uptake)		−2.60	−2.60
$\varepsilon^{202}Hg_{ocs-atm\ (0-0)}$ (surface marine Hg^0 volatilization)		−0.45	−0.45
Source $\delta^{202}Hg$ (‰) input			
Natural emissions		−0.76	−0.76
Anthropogenic emissions		P50[a]	P50[a]
Anthropogenic river discharges		−0.49	−0.49
$\delta^{202}Hg$ (‰) in modern Earth's reservoirs			
Hg^0_{atm}	0.10 ± 0.65	−1.02	−0.11
Hg^{II}_{atm}	−0.41 ± 0.48	0.00	−0.61
Hg_{tf}[b]		−2.06	−1.75
Hg_{ts}[c]	−1.39 ± 0.43	−1.11	−1.22
Hg_{ta}		0.26	−0.40
Hg^0_{ocs}		−0.23	−0.31
Hg^{II}_{ocs}		0.57	0.49
Hg^P_{ocs}		−0.13	−0.18
Hg^0_{oci}		−0.52	−0.59
Hg^{II}_{oci}		0.27	0.20
Hg^P_{oci}		−0.15	−0.21
Hg^0_{ocd}		−0.42	−0.50
Hg^{II}_{ocd}		0.16	0.09
Hg^P_{ocd}		−0.15	−0.21

[a] Median value of all-time anthropogenic Hg emissions to the atmosphere from 2000 BCE to 2010.
[b] Observed value is represented by foliage/litter (−2.56‰ ± 0.64‰) and organic surface soils (−1.79‰ ± 0.45‰).
[c] Observed value is represented by mineral soils (−1.39‰ ± 0.43‰).

($E^{199}Hg = −0.25‰ ± 0.05$, 1σ) (Sun et al., 2016a). This positive $\varepsilon^{202}Hg$ is unusual, as it is the first time that kinetic isotope fractionation shows enrichment of the less reactive heavy isotopes in the product Hg^{II}. The reaction of $Hg^0 + $ -Cl was also studied by Sun et al. (2016a), and was found to induce MDF ($\varepsilon^{202}Hg = −0.59‰ ± 0.03‰$, 1σ), odd-MIF ($E^{199}Hg = −0.37‰ ± 0.06‰$, 1σ) and a small amount of even-MIF ($E^{200}Hg = 0.06‰ ± 0.01‰$, 1σ). Here the reactant Hg^0 became enriched in the heavy and odd Hg isotopes, but also depleted in the even Hg isotopes. However, the odd-MIF of $Hg^0 + Cl$ showed a $\Delta^{199}Hg/\Delta^{201}Hg$ slope of 1.9, which is significantly higher than the slopes known for experimental MIE (1.0–1.3) (Bergquist and Blum, 2007; Zheng and Hintelmann, 2009) and NVE (~1.6) (Estrade et al., 2009; Ghosh et al., 2013). Both unusual observations on Hg isotope fractionation by $Hg^0 + Cl$ and $Hg^0 + Br$ pathways question their relevance for interpreting natural observations. Atmospheric Hg^0 photo-oxidation pathways are currently not well understood as the Hg^{II} products have not been identified. Current global Hg models however suggest that Br rather than Cl radicals are the main oxidants (Holmes et al., 2010; Horowitz et al.,

2017). Therefore, our standard model uses MDF and odd-MIF enrichment factors associated with atmospheric Hg^0 photo-oxidation via the $Hg^0 + Br$ pathway from Sun et al., 2016a. As shown in Horowitz et al. (2007), the $Hg^0 + Br$ pathway has a second oxidation step that may involve NO_2 and HO_2. However, we don't know any Hg isotope enrichment factors for this step, implying that the used enrichment factor for $Hg^0 + Br$ pathway in our model has a large uncertainty.

2.2.2.2. Reduction of aqueous dissolved Hg^{II}. Reduction of Hg^{II} bound to dissolved organic matter (DOM) is extensively studied in laboratory-controlled experiments (Bergquist and Blum, 2007; Kritee et al., 2007, 2008; Yang and Sturgeon, 2009; Zheng and Hintelmann, 2009, 2010a; Rose et al., 2015). Biotic and abiotic (photochemical and non-photochemical) reduction pathways exhibit distinct Hg isotope fractionation trajectories. MDF occurs in all these types of reduction, with a consistent enrichment of light Hg isotopes in the product Hg^0. Additionally, abiotic Hg^{II} reduction can induce characteristic MIF via MIE (photochemical) (Bergquist and Blum,

Table 2
Observed and simulated $\Delta^{199}Hg$ (‰) in the Earth's reservoirs by standard and fitted odd-MIF models (the fitted enrichment factors are shown in bold).

Enrichment factor (‰)	Observed mean ± 1SD	Model simulation Standard	#1	#2
$E^{199}Hg_{atm\ (0-II)}$ (atmospheric Hg^0 oxidation, photo-)		−0.25	−0.25	−0.25
$E^{199}Hg_{ocean\ (0-II)}$ (marine Hg^0 oxidation, photo-)		0.00	0.00	0.00
$E^{199}Hg_{atm\ (II-0)}$ (atmospheric Hg^{II} reduction, photo-)		−2.70	**−1.75**	**−1.75**
$E^{199}Hg_{ocean\ (II-0)}$ (marine Hg^{II} reduction, photo-)		−2.70	**0.55**	**0.00**
$E^{199}Hg_{ter\ (II-0)}$ (terrestrial Hg^0 emission, photo-)		1.00	1.00	**5.00**
$E^{199}Hg_{ter\ (II-0)}$ (terrestrial Hg^0 emission, nonphoto-)		0.20	0.20	**5.00**
Source $\Delta^{199}Hg$ (‰) input				
Natural emissions		0.00	0.00	0.00
Anthropogenic emissions		P50[a]	P50[a]	P50[a]
Anthropogenic river discharges		0.00	0.00	0.00
$\Delta^{199}Hg$ (‰) in modern Earth's reservoirs				
Hg_{atm}^0	−0.11 ± 0.12	−1.67	−0.11	−0.11
Hg_{atm}^{II}	0.39 ± 0.28	−0.58	0.41	0.40
Hg_{tf}[b]		−1.27	0.05	−0.30
Hg_{ts}[c]	−0.25 ± 0.14	−0.92	0.20	−0.24
Hg_{ta}		−0.32	0.37	0.30
Hg_{ocs}^0		−1.46	0.33	0.18
Hg_{ocs}^{II}		1.23	−0.21	0.18
Hg_{ocs}^P		0.90	−0.16	0.12
Hg_{oci}^0		−1.12	0.25	0.15
Hg_{oci}^{II}		1.53	−0.28	0.15
Hg_{oci}^P		1.04	−0.19	0.13
Hg_{ocd}^0		−0.31	0.10	0.17
Hg_{ocd}^{II}		1.35	−0.24	0.16
Hg_{ocd}^P		1.04	−0.19	0.13

[a] Median value of all-time anthropogenic Hg emissions to the atmosphere from 2000 BCE to 2010.
[b] Observed value is represented by foliage/litter (−0.31‰ ± 0.13‰) and organic surface soils (−0.25‰ ± 0.14‰).
[c] Observed value is represented by mineral soils (−0.25‰ ± 0.14‰).

2007; Zheng and Hintelmann, 2009) or NVE (non-photochemical) (Zheng and Hintelmann, 2010b). Microbial Hg^{II} reduction experiments showed that $\varepsilon^{202}Hg$ varies from −0.4‰ ± 0.2‰ (1σ) to −2.0‰ ± 0.2‰ (1σ), depending on the bacterial species and substrate Hg^{II} concentrations (Kritee et al., 2007, 2008). We assume that the natural bacteria un-adapted to high Hg concentrations are most representative for marine biota. Therefore, we choose a value of −0.4‰ for $\varepsilon^{202}Hg$ associated with marine, biotic Hg^{II} reduction, which is at the lower end of the range reported for microbial Hg^{II} reduction. Many photo-reduction experiments of Hg^{II}-DOM indicated that the odd Hg isotopes are preferentially enriched in the reactant Hg^{II} (Bergquist and Blum, 2007; Yang and Sturgeon, 2009; Zheng and Hintelmann, 2009; Rose et al., 2015). The large, positive $\Delta^{199}Hg$ values observed in wet deposition (Gratz et al., 2010; Chen et al., 2012; Sherman et al., 2012, 2015; Demers et al., 2013; Donovan et al., 2013; Wang et al., 2015; Yuan et al., 2015; Enrico et al., 2016) and coastal seawater samples (Štrok et al., 2014, 2015) suggest that photo-reduction of Hg^{II} in the atmosphere likely enrich odd Hg isotopes in the residual Hg^{II}. The enrichment factors reported for Hg^{II}-DOM photo-reduction experiments are very variable for different Hg/DOC ratios. The Zheng and Hintelmann (2009)'s experiment with lowest Hg/DOC ratio (35 ng mg⁻¹) studied so far is most representative for natural systems. We therefore use its enrichment factors ($\varepsilon^{202}Hg = -0.77$‰ ± 0.18‰; $E^{199}Hg = -2.75$‰ ± 0.14‰, 1σ) for Hg^{II} photo-reduction in atmospheric and oceanic reservoirs. Terrestrial Hg is mainly bound to sbndSH (thiol) ligands of organic matter in soils and in forms of thiolate complex ($Hg(SR)_2$) or Hg-S nanoparticulate in plant leaves (Skyllberg et al., 2006; Manceau et al., 2018). Zheng and Hintelmann (2010a) showed that the photo-reduction of Hg^{II} bound to low molecular weight -SH ligands is associated with a depletion of odd Hg isotopes in the reactant Hg^{II}. The enrichment factors ($\varepsilon^{202}Hg = -1.32$‰ ± 0.04‰; $E^{199}Hg = 1.02$‰ ± 0.02‰, 1σ) associated with photo-reduction of Hg^{II} bound to cysteine (−SH) from Zheng and Hintelmann (2010a) are extrapolated to terrestrial Hg^{II} photo-reduction based on their similar Hg bonding environments. Additionally, a previous Hg isotope MIF model by Sonke (2011) also suggested that soil Hg^{II} photo-reduction most likely depletes odd isotopes in terrestrial reservoir, and gave a best-fitted $E^{199}Hg$ of 1.4‰. Nevertheless, we have no experimental evidences for photochemical MIF occurring in upper soils. Following Jiskra et al. (2015), the enrichment factors ($\varepsilon^{202}Hg = -1.52$ ± 0.03‰; $E^{199}Hg = 0.18$‰ ± 0.03‰, 1σ) determined by Zheng and Hintelmann (2010b) are used for non-photochemical reduction of terrestrial Hg^{II}.

Table 3
Observed and simulated $\Delta^{200}Hg$ (‰) in the Earth's reservoirs by standard and fitted even-MIF models (the fitted rate coefficients are shown in bold).

Enrichment factor (‰)	Observed mean ± 1SD	Model simulation			
		Standard	#1	#2	#3
$E^{200}Hg_{atm\ (0-II)}$ (atmospheric Hg^0 oxidation, photo-)		0.05	0.22	0.22	0.22
Source $\Delta^{200}Hg$ (‰) input					
Natural emissions		0.00	0.00	0.00	0.00
Anthropogenic emissions		0.00	0.00	0.00	0.00
Anthropogenic river discharges		0.00	0.00	0.00	0.00
Hg mass transfer rate coefficient (yr^{-1})					
$\times\ k_{atm\ (0-II)}$ (atmospheric Hg^0 oxidation, photo-)		1	1	1	1
$\times\ k_{atm\ (II-0)}$ (atmospheric Hg^{II} reduction, photo-)		1	1	**12**	**6**
$\times\ k_{ter\ (II-0)}$ (terrestrial Hg^0 emission)		1	1	1	1
$\times\ k_{atm-ter\ (0-II)}$ (atmospheric Hg^0 dry deposition, foliar uptake)		1	1	1	**2.5**
$\Delta^{200}Hg$ (‰) in modern Earth's reservoirs					
Hg_{atm}^0	−0.04 ± 0.05	−0.03	−0.13	−0.04	−0.04
Hg_{atm}^{II}	0.17 ± 0.08	0.02	0.08	0.17	0.16
$Hg_{tf}^{\ a}$		−0.01	−0.04	−0.02	−0.02
$Hg_{ts}^{\ b}$	0.02 ± 0.04	0.00	0.02	0.01	0.00
Hg_{ta}		0.02	0.09	0.13	0.12
Hg_{ocs}^0		0.00	0.01	0.01	0.03
Hg_{ocs}^{II}		0.00	0.01	0.01	0.03
Hg_{ocs}^P		0.00	0.01	0.01	0.02
Hg_{oci}^0		0.00	0.01	0.01	0.02
Hg_{oci}^{II}		0.00	0.01	0.01	0.02
Hg_{oci}^P		0.00	0.01	0.01	0.02
Hg_{ocd}^0		0.00	0.01	0.01	0.02
Hg_{ocd}^{II}		0.00	0.01	0.01	0.02
Hg_{ocd}^P		0.00	0.01	0.01	0.02

[a] Observed value is represented by foliage/litter (−0.01‰ ± 0.05‰) and organic surface soils (−0.01‰ ± 0.03‰).

[b] Observed value is represented by mineral soils (0.02‰ ± 0.04‰).

2.2.2.3. Sorption of dissolved Hg^{II} onto particles. The dissolved Hg^{II} sorption was shown to associate with an enrichment in light Hg isotopes by −0.30‰ ± 0.04‰ (1σ) to −0.44‰ ± 0.04‰ (1σ) to the mineral surfaces (Jiskra et al., 2012), and −0.53‰ ± 0.08‰ (1σ) to −0.62‰ ± 0.09‰ (1σ) to the -SH ligands (Wiederhold et al., 2010) in $\delta^{202}Hg$. Insignificant to small odd-MIF (<0.1‰ in $\Delta^{199}Hg$) was also observed for both Hg^{II} sorption experiments. We therefore chose a value of −0.50‰ for $\varepsilon^{202}Hg$ and of 0.00‰ for $E^{199}Hg$ for the partitioning of marine dissolved Hg^{II} to Hg^P.

2.2.2.4. Evasion of dissolved gaseous Hg^0. The laboratory-controlled experiments showed that volatilization of dissolved Hg^0 from solution into the atmosphere enriches the light Hg isotopes in product gaseous Hg^0, with reported $\varepsilon^{202}Hg$ values of −0.44‰ ± 0.02‰ (1σ) and −0.47‰ ± 0.01‰ (1σ) (Zheng et al., 2007). No odd-MIF was observed during this experiment. Here, we use a value of −0.45‰ to represent the $\varepsilon^{202}Hg$ associated with dissolved Hg^0 evasion from the surface ocean.

2.2.2.5. Plant uptake of atmospheric Hg^0. Enrico et al. (2016) estimated an empirical $\varepsilon^{202}Hg$ of −2.6‰ for foliar Hg^0 uptake based on the difference in Hg concentrations

and $\delta^{202}Hg$ values of atmospheric Hg^0 between a peatland and the adjacent open mountain. This value agrees well with the $\delta^{202}Hg$ difference (−3‰ to −2‰) between atmospheric gaseous Hg (primarily Hg^0) and co-located plant leaves reported in most studies (Demers et al., 2013; Yin et al., 2013; Enrico et al., 2016; Yu et al., 2016; Obrist et al., 2017). Here, the value of −2.6‰ for foliar Hg^0 uptake is used for atmospheric Hg^0 dry deposition, following the notion that vegetation uptake is the dominant dry deposition pathway over terrestrial surfaces (Jiskra et al., 2018). Up to 0.3‰ negative shift in $\Delta^{199}Hg$ was observed in plant leaves relative to atmospheric Hg^0 (Demers et al., 2013; Yu et al., 2016; Zheng et al., 2016), which was interpreted as photo-reduction of Hg^{II} bound to sbndSH on foliage (Demers et al., 2013) and parameterized in the model as discussed above. A similar offset in $\Delta^{199}Hg$ was also observed during photo-microbial reduction of algal intracellular Hg^{II} (Kritee et al., 2018).

3. OVERVIEW OF HG ISOTOPE COMPOSITIONS IN EARTH'S RESERVOIRS

To compare simulated Hg isotope compositions by the Hg isotope box model with observations, we established a database of Hg isotope compositions measured in Earth's
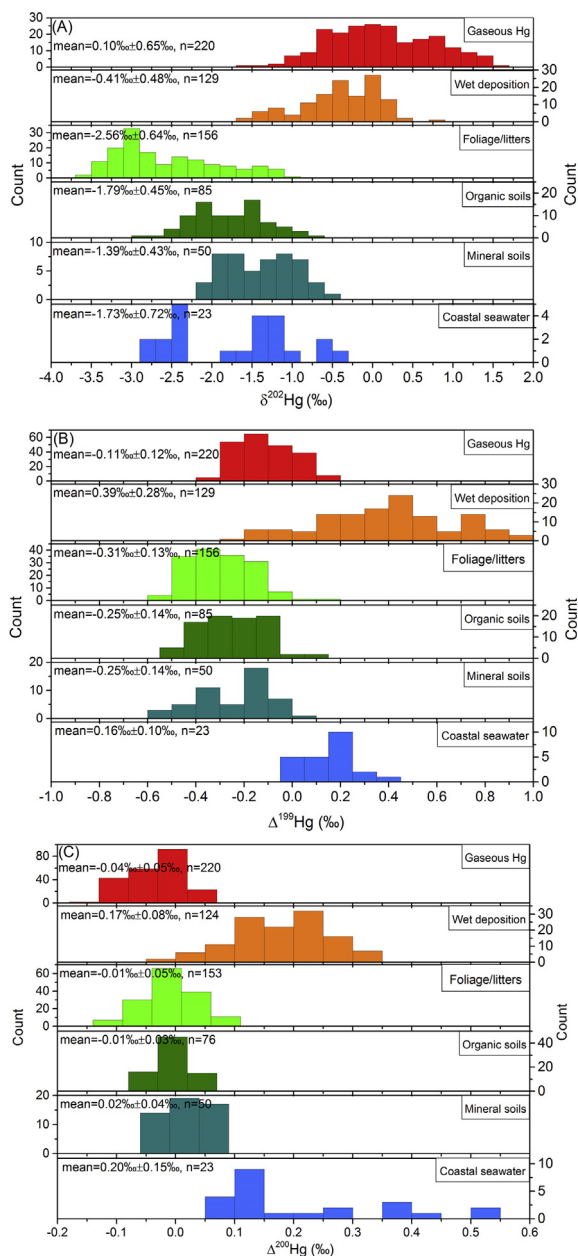
Fig. 2. Summary of published δ^{202}Hg (A), Δ^{199}Hg (B) and Δ^{200}Hg (C) in the atmospheric, terrestrial and oceanic reservoirs. Data sources: atmospheric gaseous Hg (Gratz et al., 2010; Sherman et al., 2010; Demers et al., 2013, 2015; Enrico et al., 2016; Fu et al., 2016; Yu et al., 2016; Xu et al., 2017); wet deposition without direct anthropogenic influences (Gratz et al., 2010; Chen et al., 2012; Sherman et al., 2012; Demers et al., 2013; Donovan et al., 2013; Sherman et al., 2015; Wang et al., 2015; Yuan et al., 2015; Enrico et al., 2016); folaige/litter, organic and mineral soil (Demers et al., 2013; Zhang et al., 2013; Jiskra et al., 2015; Enrico et al., 2016; Yu et al., 2016; Zheng et al., 2016; Wang et al., 2017); coastal seawater (Štrok et al., 2014, 2015). Samples with extreme δ^{202}Hg or Δ^{199}Hg or Δ^{200}Hg were removed based on statistical outlier analysis where their values higher than 3rd quartile + 1.5 × IQR (the interquartile range) or lower than 1st quartile - 1.5 × IQR are deemed as outliers.

reservoirs. Fig. 2 presents the statistic histograms for published values of δ^{202}Hg (A), Δ^{199}Hg (B) and Δ^{200}Hg (C) in the atmospheric, terrestrial and oceanic reservoirs.

3.1. Atmosphere

Due to difficulty in the separation of gaseous Hg^0 from gaseous Hg^{II} during atmospheric Hg species sampling, they are commonly collected together as total gaseous Hg. The bulk Hg isotope composition of total gaseous Hg is usually used to represent that of elemental Hg^0_{atm}, due to the small fraction of gaseous Hg^{II} (<5%) in the atmospheric boundary layer (Gratz et al., 2010; Sherman et al., 2010; Demers et al., 2013, 2015; Enrico et al., 2016; Fu et al., 2016; Yu et al., 2016; Xu et al., 2017). The background levels of gaseous Hg^{II} and particulate-bound Hg^P are too low to precisely measure their isotope compositions. Wet deposition (rain or snow) scavenges both water-soluble gaseous Hg^{II} and particulate-bound Hg^P (Keeler et al., 1995; Lindberg and Stratton, 1998; Yuan et al., 2018). We assume that the Hg isotope composition in wet deposition (Gratz et al., 2010; Chen et al., 2012; Sherman et al., 2012, 2015; Demers et al., 2013; Donovan et al., 2013; Wang et al., 2015; Yuan et al., 2015; Enrico et al., 2016) is representative for atmospheric oxidized Hg^{II}_{atm} comprised of gaseous and particulate forms in the model.

As shown in Fig. 2A–B, Hg^0_{atm} is ∼0.5‰ higher than Hg^{II} in δ^{202}Hg (0.10‰ ± 0.65‰ vs. −0.41‰ ± 0.48‰, 1σ), but is ∼0.5‰ lower than Hg^{II} in Δ^{199}Hg (−0.11‰ ± 0.12‰ vs. 0.39‰ ± 0.28‰, 1σ). Significant and positive Δ^{200}Hg observed in Hg^{II}_{atm} (0.17‰ ± 0.08‰, 1σ) is balanced by the small and negative Δ^{200}Hg in Hg^0_{atm} (−0.04 ± 0.05‰, 1σ) (Fig. 2C). Significant Hg isotope differences are observed between Hg^0_{atm} samples collected from rural sites in Europe/North America and mostly urban-industrial sites in China. Hg^0_{atm} in Europe/North America (δ^{202}Hg = 0.61‰ ± 0.44‰; Δ^{199}Hg = −0.20‰ ± 0.08‰, Δ^{200}Hg = −0.07‰ ± 0.05‰, 1σ, n = 98) (Gratz et al., 2010; Sherman et al., 2010; Demers et al., 2013, 2015; Enrico et al., 2016; Fu et al., 2016) is more enriched in heavy and depleted in odd Hg isotopes than China (δ^{202}Hg = −0.30‰ ± 0.48‰; Δ^{199}Hg = −0.04‰ ± 0.09‰, Δ^{200}Hg = −0.01‰ ± 0.03‰, 1σ, n = 122) (Yu et al., 2016; Xu et al., 2017). This difference may be explained by a higher contribution of Hg from primary anthropogenic sources in the Chinese samples, reflected also in higher Hg concentrations in China compared to Europe/North America. The regional differences are not considered in our global Hg box model.

3.2. Terrestrial reservoir

We compiled Hg isotope compositions reported in forest ecosystem including foliage, litter, organic and mineral soil (Demers et al., 2013; Zhang et al., 2013; Jiskra et al., 2015; Enrico et al., 2016; Wang et al., 2017; Yu et al., 2016; Zheng et al., 2016). δ^{202}Hg in the terrestrial reservoir increases significantly from foliage/litter (−2.56‰ ± 0.64‰, 1σ,

n = 156) to organic surface soils (−1.79‰ ± 0.45‰, 1σ, n = 85) and to mineral soil (−1.39‰ ± 0.43‰, 1σ, n = 50) (Fig. 2A). Δ^{199}Hg only shows a small increase from foliage/litter (−0.31‰ ± 0.13‰, 1σ, n = 156) to organic surface soil (−0.25‰ ± 0.14‰, 1σ, n = 85) and mineral soil (−0.25‰ ± 0.14‰, 1σ, n = 50) (Fig. 2B). No significant anomalies in Δ^{200}Hg were observed for the terrestrial reservoirs (Fig. 2C). Foliage and litters collected in China (δ^{202}Hg = −2.95‰ ± 0.36‰; Δ^{199}Hg = −0.34‰ ± 0.12‰, 1σ, n = 57) (Yu et al., 2016; Wang et al., 2017) are also significantly different from those collected in Europe/North America (δ^{202}Hg = −1.89‰ ± 0.44‰; Δ^{199}Hg = −0.25‰ ± 0.12‰, 1σ, n = 99) (Demers et al., 2013; Zhang et al., 2013; Jiskra et al., 2015; Enrico et al., 2016; Zheng et al., 2016). Thus, foliage/litter is likely biased towards low mean δ^{202}Hg value, because the database contains >60% of Chinese samples that are characterized by very negative δ^{202}Hg.

3.3. Ocean

Low Hg levels in ocean waters make measurements of Hg isotope ratios very challenging and therefore only limited data exist. Štrok et al. (2014) reported the first analyses of coastal seawater samples, and showed that δ^{202}Hg varies from −1.5‰ to −0.5‰ with small, positive Δ^{199}Hg (−0.01‰ to 0.14‰) and Δ^{200}Hg (0.05–0.53‰). A further study by Štrok et al. (2015) showed that the coastal filtered seawater near the Canadian Arctic Archipelago had more negative δ^{202}Hg (−2.85% to −1.10%), and also positive Δ^{199}Hg (0.17–0.29‰) and Δ^{200}Hg (0.05–0.52‰). Dissolved Hg^{II} is the primary Hg pool in the ocean, and is likely the main Hg form in these reported seawater samples (Lamborg et al., 2014; Zhang et al., 2014). Up until now, Hg isotope data for open ocean waters are not reported. Blum et al. (2013) proposed that the dissolved Hg^{II} in the open Pacific Ocean likely had small positive δ^{202}Hg and Δ^{199}Hg, similar to the Pacific coastal rainwater (δ^{202}Hg = 0–0.2‰; Δ^{199}Hg = 0.25–0.35‰) (Sherman et al., 2012; Donovan et al., 2013). It is noted that seawater in coastal and shelf areas might be significantly affected by Hg inputs from terrestrial reservoirs, while the open ocean mainly receives Hg from atmospheric deposition (Holmes et al., 2010; Amos et al., 2014).

Therefore, based on the availability of Hg stable isotope measurements, we consider the Hg isotope composition of the atmospheric reservoir as the primary observational constraint followed by the terrestrial reservoir. The Hg isotope composition of the oceanic reservoir is used as the least well-known constraint. In the following, the simulated results of the models are first compared against the Hg isotope composition of atmospheric reservoir followed by those of terrestrial and oceanic reservoirs.

4. MODELLING RESULTS AND EVALUATION

The Hg isotope box model simulation is first run for MDF, odd-MIF and even-MIF until natural steady-state in both Hg masses (i.e. $dM_i/dt = 0$) and Hg isotope compositions (i.e. $d(\delta^{202}Hg_i)/dt = 0$, $d(\Delta^{199}Hg_i)/dt = 0$ and d

($\Delta^{200}Hg_i)/dt = 0$) of all reservoirs. The initial spin-up uses geogenic Hg emissions to the atmosphere only (S = 90 Mg a^{-1}) with a constant Hg isotope composition ($\delta^{202}Hg_s = -0.76‰$; $\Delta^{199}Hg_s = 0.00‰$; $\Delta^{200}Hg_s = 0.00‰$). Then, following Amos et al. (2014), the reservoir Hg masses and Hg isotope compositions in natural steady-state are used as the initial conditions for the standard model run from 2000 BCE until present (2010). In the standard model all-time anthropogenic Hg emissions to the atmosphere are introduced with a time-dependent Hg isotope composition (1850–2010: data from Sun et al. (2016b); pre-1850: $\delta^{202}Hg_s = -0.91‰$; $\Delta^{199}Hg_s = 0.00‰$; $\Delta^{200}Hg_s = 0.00‰$) and direct anthropogenic Hg discharges into rivers with a constant Hg isotope composition ($\delta^{202}Hg_s = -0.49‰$; $\Delta^{199}Hg_s = 0.00‰$; $\Delta^{200}Hg_s = 0.00‰$) (Tables 1–3). The simulated Hg budgets and isotope compositions of environmental reservoirs (boxes) are not at steady-state due to human perturbations since 2000 BCE.

Table EA-3 lists the simulated Hg sizes in various reservoirs under natural steady-state and in 1850 and 2010. The simulated present-day (2010) Hg size is 5500 Mg for atmosphere, 12,300 Mg (i.e. 1.14 pM) for the upper ocean (surface and intermediate ocean) and 250,000 Mg for the terrestrial soils. The atmospheric Hg deposition in modern days (1990–2010) is elevated by a factor of 3.8 relative to the pre-industrial period (1760–1880). These data are comparable to those derived from contemporary measurements and various models (atmosphere: 4600–5600 Mg; upper ocean: 0.5–2.0 pM; terrestrial soils: >200,000; pre-industrial Hg enrichment factor: 2–5) (Lamborg et al., 2002; Biester et al., 2007; Sunderland and Mason, 2007; Selin et al., 2008; Mason et al., 2012; Amos et al., 2013, 2014; Hararuk et al., 2013; Horowitz et al., 2014; Lamborg et al., 2014; Zhang et al., 2014; Bowman et al., 2015; Horowitz et al., 2017).

Fig. 3 shows that the simulated modern-day δ^{202}Hg and Δ^{199}Hg values in the atmospheric, terrestrial and oceanic reservoirs are very different from their observed isotope compositions. For example, the standard model predicts that δ^{202}Hg values of Hg^{II}_{atm} are more than 1‰ higher than Hg^0_{atm}, which is contrary to the observations of higher δ^{202}Hg values of gaseous Hg^0 compared to wet deposition (Table 1). The simulated atmospheric and terrestrial Δ^{199}Hg values are underestimated by over 1‰ compared to their observed values (Table 2). The simulated Δ^{200}Hg values are too small to explain the observed large Δ^{200}Hg in the wet deposition (Table 3). Thus, it appears that the direct use of experimentally determined Hg isotope enrichment factors is unrealistic or some key Hg isotope enrichment factors are missing in the standard Hg isotope model. To a lesser extent, the uncertainties in source Hg isotope compositions and Hg mass transfer processes in our Hg cycling box model also potentially bias the simulated output.

5. DISCUSSION ON HG ISOTOPE BOX MODEL

In the following, we first discuss how the source Hg isotope uncertainties affect the simulated Hg isotope compositions. Then, we test the sensitivity of simulated Hg isotope
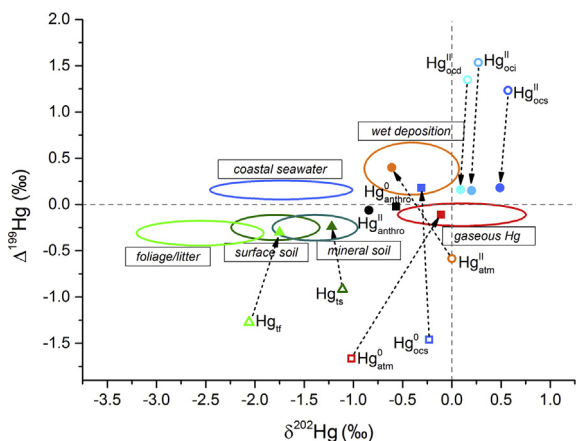
Fig. 3. The simulated modern-day (2010) $\delta^{202}Hg$ and $\Delta^{199}Hg$ in atmospheric Hg_{atm}^0, atmospheric Hg_{atm}^{II}, fast terrestrial Hg_{tf}, slow terrestrial Hg_{ts}, upper oceanic Hg_{ocs}^0 and oceanic Hg^{II} (surface Hg_{ocs}^{II}, intermediate Hg_{oci}^{II}, deep Hg_{ocd}^{II}) reservoirs using the MDF and odd-MIF standard models (hollow symbols), and the MDF model #1 (i.e. fractionation sign inversion of atmospheric Hg^0 photo-oxidation by Br) and odd-MIF model #2 (i.e. strong fractionation for terrestrial Hg^{II} reduction) (filled symbols) (Tables 1 and 2). The observed $\delta^{202}Hg$ and $\Delta^{199}Hg$ values are indicated by ellipses where the center, horizontal axe and vertical axe denote the means of $\delta^{202}Hg$ and $\Delta^{199}Hg$, 1SD on $\delta^{202}Hg$ and 1SD on $\Delta^{199}Hg$, respectively. The mean anthropogenic isotope compositions of Hg_{anthro}^0 and Hg_{anthro}^{II} into atmosphere are shown in black filled symbols. The arrows indicate the shift in Hg isotope signatures from the standard model to the fitted models.

compositions to Hg isotope enrichment factors, with the aim of finding the best-fitted enrichment factors that reproduce the observed Hg isotope compositions. Lastly, we examine the sensitivity of simulated Hg isotope compositions to some key but controversial Hg mass transfer processes.

5.1. Uncertainties in source Hg isotope compositions

The Hg input inventory for the Hg isotope model include three categories: geogenic Hg emissions to the atmosphere, all-time anthropogenic Hg emissions to the atmosphere and anthropogenic Hg discharges to rivers and ultimately oceans. $\Delta^{199}Hg$ and $\Delta^{200}Hg$ values in all these sources are very small, and are generally around zero within the measurement uncertainty ($\pm0.10‰$). Setting $\Delta^{199}Hg$ values of all-time anthropogenic Hg emissions as zeros has no significant effect (<0.03‰ increase) on the simulated $\Delta^{199}Hg$ in all the Earth's reservoirs. Thus, we only discuss the model sensitivity to the uncertainties of source $\delta^{202}Hg$ values.

Due to the large amount of anthropogenic Hg released, any uncertainty in geogenic $\delta^{202}Hg$ only has a very little effect on the modern reservoir $\delta^{202}Hg$ values. Varying geogenic $\delta^{202}Hg$ by 1‰ only changes <0.1‰ in the modern $\delta^{202}Hg$ values of reservoirs except for the armored terrestrial reservoir and deep ocean. Similarly, the simulated reservoir $\delta^{202}Hg$ values are also insensitive to the $\delta^{202}Hg$ variation in anthropogenic Hg discharges to rivers from

1850 to 2010. This is because >90% of riverine Hg exists as Hg^P of which ∼70% is thought to be buried in the shelf and coastal areas before entering into open ocean (Amos et al., 2014; Zhang et al., 2015). Varying the $\delta^{202}Hg$ values of anthropogenic riverine discharges between mean (−0.5‰) and mean-1σ (−0.9‰) or mean + 1σ (−0.1‰) only slightly changes modern reservoir $\delta^{202}Hg$ values (<0.1‰ for atmospheric and terrestrial reservoirs; 0.10–0.15‰ for oceanic reservoirs). In contrast, the simulated reservoir $\delta^{202}Hg$ values are very sensitive to the $\delta^{202}Hg$ variation in all-time anthropogenic Hg emissions. The use of the lower (P10) or upper (P90) boundary $\delta^{202}Hg$ values (Sun et al., 2016b) changes the modern reservoir $\delta^{202}Hg$ values by 0.12–0.27‰. Taken together, the $\delta^{202}Hg$ uncertainties of Hg release sources may account for up to 0.5‰ variation in $\delta^{202}Hg$ values of modern Earth's reservoirs.

5.2. Fitting of Hg isotope enrichment factors

The fitting of Hg isotope enrichment factors adopts the following steps on basis of the observational constraints as discussed in Section 3. (1) The enrichment factors associated with atmospheric redox processes are initially fitted to reproduce the relative difference of observed Hg isotope compositions between Hg_{atm}^0 and Hg_{atm}^{II}. (2) The enrichment factors associated with terrestrial and oceanic redox processes are then fitted to match the absolute values of observed Hg isotope compositions of Hg_{atm}^0 and Hg_{atm}^{II}. (3) The simulated Hg isotope compositions of terrestrial and upper oceanic Hg^{II} are compared with their observed values to find the optimized combination of enrichment factors. Model fitting runs are indicated as 'model #1-x' in contrast with the 'standard model' that is only based on published enrichments factors (Tables 1–3).

5.2.1. Mass dependent fractionation (MDF) model

In the standard MDF model, both photo-reduction of Hg_{atm}^{II} and photo-oxidation of Hg_{atm}^0 enrich heavy Hg isotopes in Hg_{atm}^{II}, causing $\delta^{202}Hg_{atm}^{II}$ to be significantly higher than $\delta^{202}Hg_{atm}^0$. This is contrary to observed $\delta^{202}Hg$ in the atmosphere where $\delta^{202}Hg_{atm}^0$ exceeds $\delta^{202}Hg_{atm}^{II}$ by ∼0.5‰ (Fig. 3). Here, we optimize photo-oxidation $\varepsilon^{202}Hg_{atm\ (0-II)}$ to enrich the light Hg isotopes in the product Hg_{atm}^{II} which would be coherent with kinetic isotope fractionation theory (i.e. light isotopes are preferably enriched in products) (Hoefs, 2015; Wiederhold, 2015). We find that a value of −0.85‰ for $\varepsilon^{202}Hg_{atm\ (0-II)}$ results in ∼0.5‰ relative difference between the simulated $\delta^{202}Hg_{atm}^0$ (−0.1‰) and $\delta^{202}Hg_{atm}^{II}$ (−0.6‰) (MDF model #1 in Table 1). This suggests that the photo-oxidation $\varepsilon^{202}Hg_{atm\ (0-II)}$ based on the $Hg^0 + Br$ pathway in Sun et al. (2016a) used in the standard MDF model (discussed in section 2.2.2.1) is not representative for atmospheric Hg^0 oxidation. Although the simulated $\delta^{202}Hg_{atm}^0$ and $\delta^{202}Hg_{atm}^{II}$ are ∼0.2‰ lower than their observed values (Table 1), they are within the 0.5‰ variation attributed to the Hg input source uncertainties in $\delta^{202}Hg$. The simulated $\delta^{202}Hg_{tf}$ (−1.8‰) is higher than the average $\delta^{202}Hg$ value of Chinese foliage/litter (−3.0‰) that is affected by anthropogenic Hg^0 with low $\delta^{202}Hg$, but is similar to the average $\delta^{202}Hg$ values of European/

North American foliage/litter (−1.9‰) and global organic surface soils (−1.8‰) (Fig. 2B). The simulated $\delta^{202}Hg_{ts}$ (−1.2‰) is comparable to the global mineral soils (−1.39‰) (Fig. 2B). The simulated upper oceanic $\delta^{202}Hg^{II}$ values (0.2–0.5‰) are compatible with the slightly positive $\delta^{202}Hg$ values proposed for open surface ocean (0–0.2‰) by Blum et al. (2013). Thus, it appears that the optimization (i.e. sign inversion) of atmospheric photo-oxidation $\varepsilon^{202}Hg_{atm\ (0-II)}$ is critical to attain satisfactory simulated reservoir $\delta^{202}Hg$ values. Given the multitude of fractionating processes, further assessment of marine and terrestrial redox $\varepsilon^{202}Hg$ is difficult in the MDF model.

5.2.2. Odd-mass independent fractionation (odd-MIF) model

Compared to the observations, the odd-MIF standard model predicts too low $\Delta^{199}Hg$ values for atmospheric and terrestrial reservoirs, and too high $\Delta^{199}Hg$ values for upper oceanic Hg^{II} reservoir (Fig. 3). This is because the simulated surface ocean Hg^0_{ocs} has a very negative $\Delta^{199}Hg$ value (−1.5‰, Table 2) due to the large negative marine photo-reduction $E^{199}Hg_{ocean\ (II-0)}$ (−2.70‰), which propagates to atmospheric and terrestrial reservoirs. This effect was shown previously for a global Hg odd-MIF model by Sonke (2011), who suggested that marine Hg odd-MIF is not needed to explain global $\Delta^{199}Hg$ distribution. Additionally, the same large negative atmospheric photo-reduction $E^{199}Hg_{atm\ (II-0)}$ (−2.70‰) results in low atmospheric and terrestrial $\Delta^{199}Hg$ values as well. Therefore, $E^{199}Hg_{ocean\ (II-0)}$ and $E^{199}Hg_{atm\ (II-0)}$ are fitted to increase atmospheric and terrestrial $\Delta^{199}Hg$ values. The odd-MIF model #1 in Table 2 shows that a less strong atmospheric and marine photo-reductive odd-MIF ($E^{199}Hg_{atm\ (II-0)} = -1.75‰$; $E^{199}Hg_{ocean\ (II-0)} = 0.55‰$) results in non-biased atmospheric $\Delta^{199}Hg$ values ($\Delta^{199}Hg^0_{atm} = -0.11‰$; $\Delta^{199}Hg^{II}_{atm} = 0.41‰$). However, the simulated $\Delta^{199}Hg$ values are positive for the terrestrial reservoir and negative for the oceanic Hg^{II} reservoir (Table 2), which is inconsistent with observations on vegetation, soils and marine waters (Fig. 2B).

In the odd-MIF standard model, $E^{199}Hg_{ter\ (II-0)}$ associated with photo- and non-photo-reduction of Hg^{II} in the terrestrial reservoirs are assigned values of 1‰ (MIE) and 0.2‰ (NVE), respectively (Table 2). An increase in terrestrial reduction $E^{199}Hg_{ter\ (II-0)}$ would reduce the $\Delta^{199}Hg$ value of terrestrial reservoir and increase the $\Delta^{199}Hg$ value of the atmospheric reservoir. Here, the odd-MIF model #1 is modified to include a larger $E^{199}Hg_{ter\ (II-0)}$ value. Simulation results show that a value of 5‰ for $E^{199}Hg_{ter\ (II-0)}$ along with a less strong atmospheric and marine photo-reductive odd-MIF ($E^{199}Hg_{ocean\ (II-0)} = 0.00‰$; $E^{199}Hg_{atm\ (II-0)} = -1.75‰$) could well reproduce the observed $\Delta^{199}Hg$ values of fast/slow terrestrial and atmospheric reservoirs (odd-MIF model #2 in Table 2). However, such a large $E^{199}Hg_{ter\ (II-0)}$ value is not reported in the literature and seems implausible. This implies that the terrestrial Hg^0 emission flux in the model is incorrect (see discussion in section 5.3).

Marine Hg reduction and oxidation MIF factors are not studied experimentally. If we assume a zero value for the unknown oxidation $E^{199}Hg_{ocean\ (0-II)}$, the fitted reduction

$E^{199}Hg_{ocean\ (II-0)}$ value is also zero. If $E^{199}Hg_{ocean\ (0-II)}$ is assigned with a non-zero value, the fitted $E^{199}Hg_{ocean\ (II-0)}$ will also change to this non-zero value. This implies that $E^{199}Hg_{ocean\ (0-II)}$ and $E^{199}Hg_{ocean\ (II-0)}$ is comparable in magnitudes or that the marine photo-oxidation and photo-reduction do not necessarily produce odd-MIF as argued by Sonke (2011). Experimental or field studies of marine Hg odd-MIF are lacking thus far. A recent study did observe intracellular photomicrobial odd-MIF in laboratory incubations of marine microalga where the enrichment factor $E^{199}Hg_{(II-0)}$ was around −1‰. However, the importance of such photo-biological odd-MIF appears limited as the estimated reduction flux of 5 Mmol yr^{-1} is much smaller than estimates of the abiotic photo-reduction flux of >10,000 Mmol yr^{-1} (Zhang et al., 2015; Kritee et al., 2018).

In summary, optimization analysis of odd-MIF models suggests that a large terrestrial reduction $E^{199}Hg_{ter\ (II-0)}$ is important to model global $\Delta^{199}Hg$ distribution, and the magnitudes of odd-MIF associated with photo-oxidation and photo-reduction in the ocean are likely both very small.

5.2.3. Even-mass dependent fractionation (even-MIF) model

The even-MIF standard model does not reproduce the observed large $\Delta^{200}Hg$ in wet deposition (Fig. 2C). The even-MIF standard model used a small atmospheric photo-oxidation $E^{200}Hg_{atm\ (0-II)}$ of 0.05‰ (Table 3), a value based on the recent Hg^0 oxidation experiment (Sun et al., 2016a). Fig. EA-1 shows that the relative difference (∼0.2‰) between the observed $\Delta^{200}Hg^0_{atm}$ (−0.04‰) and $\Delta^{200}Hg^{II}_{atm}$ (0.17‰) (Fig. 2C) can only be achieved by fitting a value of 0.22‰ for $E^{200}Hg_{atm\ (0-II)}$. However, the simulated $\Delta^{200}Hg^0_{atm}$ (−0.13‰) and $\Delta^{200}Hg^{II}_{atm}$ (0.08‰) (Fig. EA-1) are still ∼0.10‰ lower than their observed values (even-MIF model #1 in Table 3). If we presume that even-MIF also occurs during marine Hg^0 photo-oxidation in the ocean and $E^{200}Hg_{ocean\ (0-II)}$ has a value of −0.2‰, the model reproduces the observed $\Delta^{200}Hg$ values of the atmospheric reservoir. However, the oceanic Hg^{II} would develop negative $\Delta^{200}Hg$ values, which are unlikely considering the observed positive $\Delta^{200}Hg$ in coastal seawater (Štrok et al., 2014, 2015) and the near-zero $\Delta^{200}Hg$ of marine sediments (Gehrke et al., 2009; Mil-Homens et al., 2013; Yin et al., 2015). Whatever the oxidative even-MIF mechanism, it appears not to operate in the aqueous marine environment. Alternatively, the even-MIF model suggests that the uncertainties in Hg mass transfer processes likely bias the simulated $\Delta^{200}Hg$ values (see below).

5.3. Uncertainties in Hg mass transfer processes

Three Hg fluxes deserve particular attention. Firstly, in the standard model, the atmospheric Hg^0_{atm} dry and Hg^{II}_{atm} wet deposition ratio to the terrestrial reservoir ($Hg^0_{atm-ter}/Hg^{II}_{atm-ter}$) has a value of 1 (Table EA-1). As discussed in the introduction section, the surface soil primarily receives Hg^0_{atm} deposition via plant uptake, with a net $Hg^0_{atm-ter}/Hg^{II}_{atm-ter}$ ratio of 2–4 (Demers et al., 2013; Jiskra et al., 2015; Enrico et al., 2016; Zheng et al., 2016;

Obrist et al., 2017). Secondly, Horowitz et al. (2017) recently implemented a fast two-step atmospheric Hg^0 oxidation mechanism in the GEOS-Chem model, reducing Hg^0 lifetime to <3 months, and requiring a significant increase of in-cloud aqueous Hg^{II} photo-reduction rate to match global Hg^0 and Hg^{II} deposition observations. Compared to the mass transfer rate coefficients for atmospheric photo-oxidation ($k_{atm\ (0-II)}$) and in-cloud photo-reduction ($k_{atm\ (II-0)}$) in our standard model, Table EA-1, both k values are increased by a factor of $\sim$2 and $\sim$7, respectively, in Horowitz et al. (2017). Thirdly, the terrestrial Hg^0 emission flux used to derive terrestrial Hg^0 emission rate coefficient ($k_{ter\ (II-0)}$) is only 160 Mg yr^{-1} (reflecting greater soil Hg retention as suggested by Amos et al., 2014) (Table EA-1), which is much lower than the value ($\sim$600 Mg yr^{-1}, from -500 Mg yr^{-1} at 37.5th percentile to 1350 Mg yr^{-1} at 67.5th percentile) established in a recent review (Agnan et al., 2016). We thus examine the sensitivity of simulated $\delta^{202}Hg$ (Fig. 4), $\Delta^{199}Hg$ (Fig. 5) and $\Delta^{200}Hg$ (Fig. 6) to the following Hg mass transfer parameters: atmospheric Hg^0 photo-oxidation $k_{atm\ (0-II)}$ (A), atmospheric Hg^{II} photo-reduction $k_{atm\ (II-0)}$ (B), $Hg^0_{atm-ter}/Hg^{II}_{atm-ter}$ ratio (C) and terrestrial Hg^0 emission $k_{ter\ (II-0)}$ (D).

As shown in Fig. 4, the simulated atmospheric Hg^0_{atm} and Hg^{II}_{atm} approach to their observed mean values when either atmospheric photo-reduction $k_{atm\ (II-0)}$ (B) or $Hg^0_{atm-ter}/Hg^{II}_{atm-ter}$ ratio (C) is slightly increased. A prominent feature of Fig. 5 is that an increase in terrestrial emission $k_{ter\ (II-0)}$ could effectively decrease terrestrial $\Delta^{199}Hg$ values (D), implying that a smaller terrestrial photo-reduction E^{199}-$Hg_{ter\ (II-0)}$ in odd-MIF model #2 (Table 2) can be fitted. If we increase $k_{ter\ (II-0)}$ by a factor of 4 (resulting in an increase of terrestrial Hg^0 emission flux from 160 to $\sim$600 Mg yr^{-1} as suggested by Agnan et al., 2016) in odd-MIF model #2, the fitted $E^{199}Hg_{ter\ (II-0)}$ can be decreased from 5‰ to a more plausible value of 2‰. This indicates that the terrestrial Hg^0 emission flux of 160 Mg yr^{-1} in the standard model (Table EA-1) may be underestimated.

Even-MIF is thought to occur during atmospheric (net) Hg^0 oxidation. We have shown in the even-MIF model #1 that a fitted value of 0.22‰ for $E^{200}Hg_{atm\ (0-II)}$ could match the relative difference between the observed $\Delta^{200}Hg^0_{atm}$ and $\Delta^{200}Hg^{II}_{atm}$, but not the absolute values. To increase simulated $\Delta^{200}Hg^0_{atm}$ (-0.13‰) and $\Delta^{200}Hg^{II}_{atm}$ (0.08‰), it requires an increase of atmospheric photo-reduction $k_{atm\ (II-0)}$ (Fig. 6B) or $Hg^0_{atm-ter}/Hg^{II}_{atm-ter}$ (Fig. 6C).

Fig. 4. Sensitivity of $\delta^{202}Hg$ values (simulated by MDF model #1 in Table 1) in modern atmospheric, terrestrial and upper oceanic Hg^{II} reservoirs to variations in atmospheric Hg^0 photo-oxidation rate coefficient ($k_{atm\ (0-II)}$) (A), atmospheric Hg^{II} photo-reduction rate coefficient ($k_{atm\ (II-0)}$) (B), atmospheric Hg dry and wet deposition ratio to the terrestrial reservoir ($Hg^0_{atm-ter}/Hg^{II}_{atm-ter}$), (C) and terrestrial Hg^0 emission rate coefficient ($k_{ter\ (II-0)}$) (D). The grey bars denote the observed atmospheric $\delta^{202}Hg$ values.
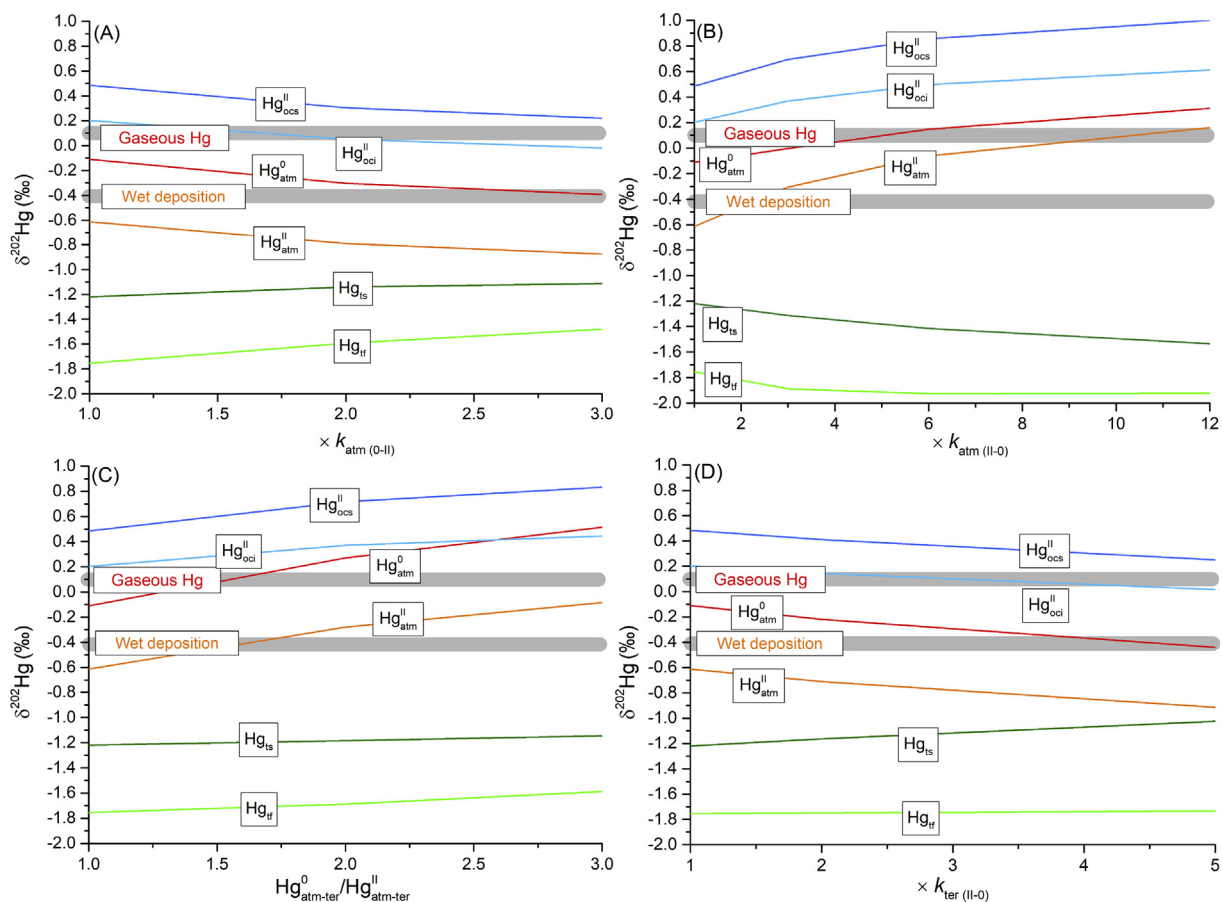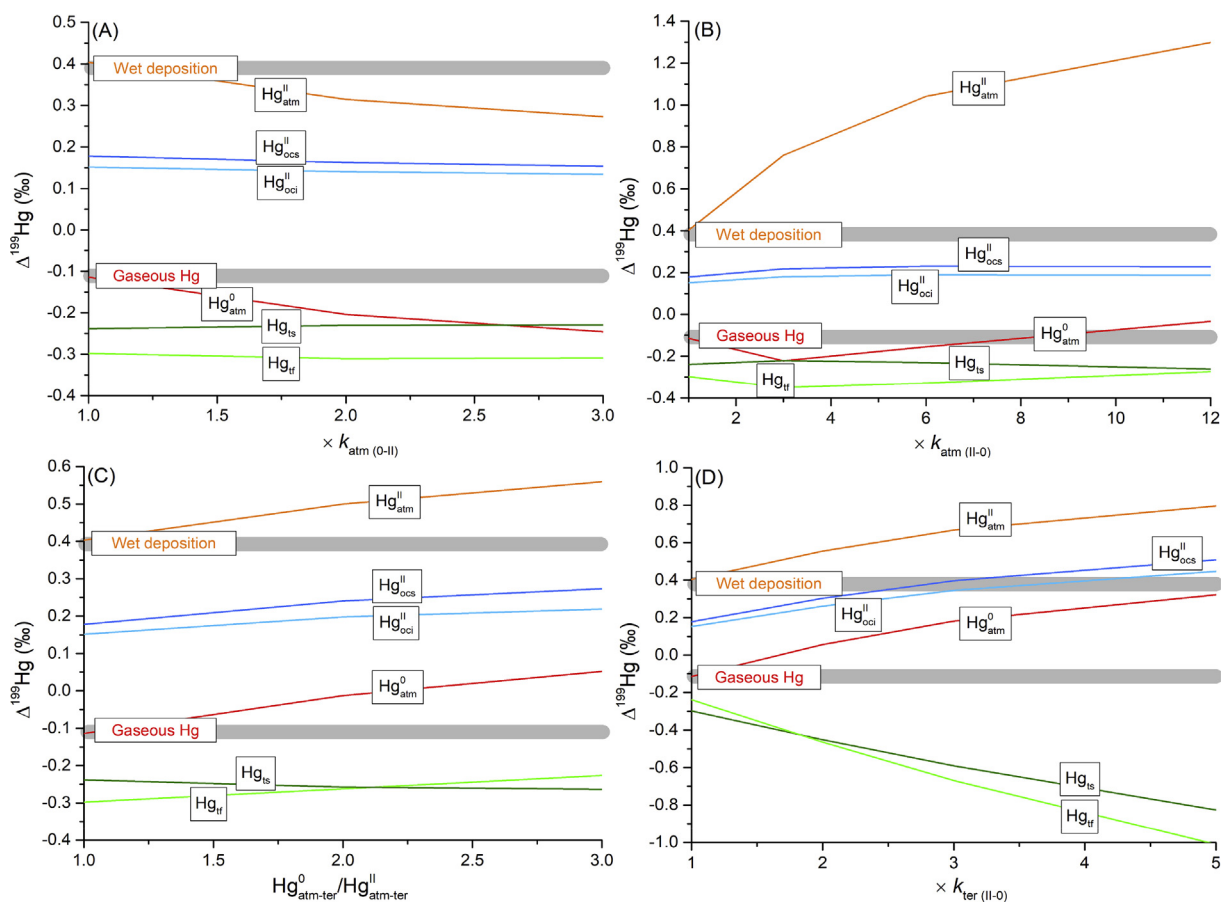
Fig. 5. Sensitivity of Δ^{199}Hg values (simulated by odd-MIF model #2 in Table 2) in modern atmospheric, terrestrial and upper oceanic Hg^{II} reservoirs to variations in atmospheric Hg^0 photo-oxidation rate coefficient ($k_{atm\ (0-II)}$) (A), atmospheric Hg^{II} photo-reduction rate coefficient ($k_{atm\ (II-0)}$) (B), atmospheric Hg dry and wet deposition ratio to the terrestrial reservoir (Hg$^0_{atm-ter}$/Hg$^{II}_{atm-ter}$), (C) and terrestrial Hg^0 emission rate coefficient ($k_{ter\ (II-0)}$) (D). The grey bars denote the observed atmospheric Δ^{199}Hg values.

Sensitivity analysis (even-MIF model #2) shows that an increase in the default atmospheric photo-reduction $k_{atm\ (II-0)}$ by a factor of 12 reproduces both Δ^{200}Hg$^0_{atm}$ (−0.04‰) and Δ^{200}Hg$^{II}_{atm}$ (0.17‰) (Fig. EA-2A; Table 3). However, the even-MIF model #2 predicts a much larger Hg$^0_{atm}$ (8500 Mg) and smaller Hg$^{II}_{atm}$ (370 Mg) reservoirs in the atmosphere, and an atmospheric THg mass about two times of modern values (4000–5600 Mg) (Fig. EA-2B) (Selin et al., 2008; Mason et al., 2012; Amos et al., 2013, 2014; Horowitz et al., 2014, 2017). A further sensitivity analysis (even-MIF model #3) shows that a 6 times larger $k_{atm\ (II-0)}$ along with a Hg$^0_{atm-ter}$/Hg$^{II}_{atm-ter}$ ratio of 2.5 (within the range of Hg$^0_{atm-ter}$/Hg$^{II}_{atm-ter}$ ratio suggested by the new plant Hg^0 uptake paradigm) also results in unbiased atmospheric Δ^{200}Hg values (Fig. EA-2A; Table 3), and a reasonable atmospheric THg budget (4500 Mg) (Fig. EA-2B). Thus, it appears that fast atmospheric Hg^0 dry deposition rate to terrestrial plants (i.e. foliar uptake, followed by intracellular oxidation, and limited re-emission, Manceau et al., 2018) is able to reconcile both MDF and MIF constraints. This reconciles with recent observations that vegetation uptake of atmospheric Hg^0

drives seasonal and diurnal dynamics of atmospheric Hg^0 (Jiskra et al., 2018).

The above discussion on Hg isotope enrichment factors and Hg mass transfer processes in our Hg isotope models indicates that MDF model #1 (fractionation sign inversion of atmospheric Hg^0 photo-oxidation by Br, Table 1, Fig. 3), odd-MIF model #2 (strong fractionation of terrestrial Hg^{II} reduction, Table 2, Fig. 3) and even-MIF #3 (enhanced in-cloud aqueous Hg^{II} photo-reduction and plant Hg^0 uptake, Table 3) could well reproduce the observed Hg isotope compositions across different Earth's reservoirs. For example, atmospheric Hg^0 source tracing studies showed that continental background and marine-influenced Hg^0 have apparently higher δ^{202}Hg values than recent anthropogenic Hg^0 emissions (Demers et al., 2015; Fu et al., 2016; Yu et al., 2016). The input of terrestrial Hg into the coastal regions explains the reported low δ^{202}Hg and Δ^{199}Hg values in the seawater, sediments and fish tissues from coastal areas (Senn et al., 2010; Perrot et al., 2012; Das et al., 2013; Li et al., 2014; Štrok et al., 2014, 2015; Yin et al., 2015). The fitted models also indicate that upper oceanic Hg^{II} reservoir has positive δ^{202}Hg (0.2–0.5‰), Δ^{199}Hg
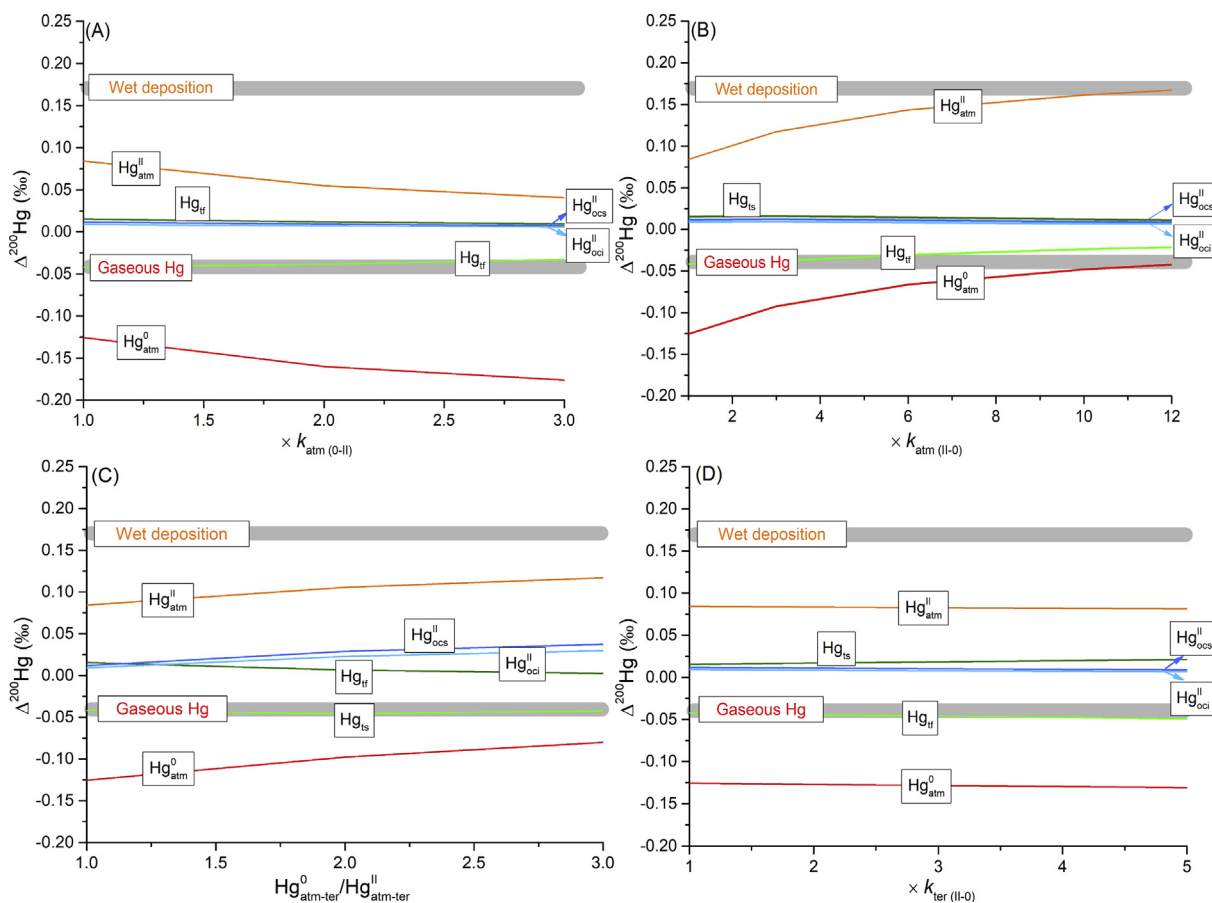
Fig. 6. Sensitivity of Δ^{200}Hg values (simulated by even-MIF model #1 in Table 3) in modern atmospheric, terrestrial and upper oceanic Hg^{II} reservoirs to variations in atmospheric Hg^0 photo-oxidation rate coefficient ($k_{\text{atm (0-II)}}$) (A), atmospheric Hg^{II} photo-reduction rate coefficient ($k_{\text{atm (II-0)}}$) (B), atmospheric Hg dry and wet deposition ratio to the terrestrial reservoir (Hg$^0_{\text{atm-ter}}$/Hg$^{II}_{\text{atm-ter}}$) (C) and terrestrial Hg^0 emission rate coefficient ($k_{\text{ter (II-0)}}$) (D). The grey bars denote the observed atmospheric Δ^{200}Hg values.

(0.1–0.2‰) and Δ^{200}Hg (0.02–0.03‰) (Fig. 3), similar to the values proposed for the open Pacific Ocean (Blum et al., 2013). Additionally, the Hg isotope difference between coastal and open ocean seawaters supports the observations that pelagic ocean fish has higher δ^{202}Hg and Δ^{199}Hg than costal and freshwater fish (Senn et al., 2010; Perrot et al., 2012; Blum et al., 2013; Li et al., 2014).

6. CONCLUDING REMARKS

We provide a mechanistic model framework to examine the controls of sources and biogeochemical processes on the Hg isotope distribution in various Earth's surface reservoirs. The ensemble of MDF, odd-MIF and even-MIF sensitivity analyses indicates that (1) the limited set of available experimentally derived MDF and MIF factors cannot explain current Hg isotope observations; (2) MDF associated with atmospheric photo-oxidation likely enriches product Hg^{II} with light Hg isotopes; (3) terrestrial reduction odd-MIF is likely significant and marine odd-MIF associated with photo-oxidation and photo-reduction is possibly negligible in magnitude; (4) the following Hg fluxes are potentially not correct in global Hg models: atmospheric

Hg^{II} photo-reduction, Hg^0 dry deposition via plant uptake, terrestrial Hg^0 emission.

Currently, the enrichment factors (or fractionation factors) used in the Hg isotope model are associated with large uncertainties, and the enrichment factors of some important Hg redox reactions (e.g. dissolved Hg^0 oxidation in the ocean) are still lacking. An important future research avenue would be the determination of these enrichment factors under experimental conditions that are more representative of natural ecosystems. Further, the assembled Hg isotope observations used for simulation evaluation are potentially biased both spatially and temporally, and show high between-site heterogeneity. More measurements of Hg isotope compositions in various biogeochemical reservoirs, particularly the open ocean, are needed, which would provide more robust constrains on the global Hg cycling.

APPENDIX A. SUPPLEMENTARY MATERIAL

Supplementary data associated with this article can be found, in the online version, at https://doi.org/10.1016/j.gca.2018.11.036.

REFERENCES

Agnan Y., Le Dantec T., Moore C. W., Edwards G. C. and Obrist D. (2016) New constraints on terrestrial surface-atmosphere fluxes of gaseous elemental mercury using a global database. *Environ. Sci. Technol.* **50**, 507–524.

Amos H. M., Jacob D. J., Streets D. G. and Sunderland E. M. (2013) Legacy impacts of all-time anthropogenic emissions on the global mercury cycle. *Global Biogeochem. Cycles* **27**, 410–421.

Amos H. M., Jacob D. J., Kocman D., Horowitz H. M., Zhang Y., Dutkiewicz S., Horvat M., Corbitt E. S., Krabbenhoft D. P. and Sunderland E. M. (2014) Global biogeochemical implications of mercury discharges from rivers and sediment burial. *Environ. Sci. Technol.* **48**, 9514–9522.

Amos H. M., Sonke J. E., Obrist D., Robins N., Hagan N., Horowitz H. M., Mason R. P., Witt M., Hedgecock I. M., Corbitt E. S. and Sunderland E. M. (2015) Observational and modeling constraints on global anthropogenic enrichment of mercury. *Environ. Sci. Technol.* **49**, 4036–4047.

Andren M. O. and Nriagu J. O. (1979) The global cycle of mercury. In *Biochemistry of Mercury in the Environment* (ed. J. O. Nriagu). Elsevier, Amsterdam, pp. 1–15.

Bagnato E., Aiuppa A., Parello F., Allard P., Shinohara H., Liuzzo M. and Giudice G. (2011) New clues on the contribution of Earth's volcanism to the global mercury cycle. *Bull. Volcanol.* **73**, 497–510.

Bagnato E., Tamburello G., Avard G., Martinez-Cruz M., Enrico M., Fu X., Sprovieri M. and Sonke J. E. (2014) Mercury fluxes from volcanic and geothermal sources: an update. *Geol. Soc. London, Spec. Publ.*, 410.

Bergquist B. A. and Blum J. D. (2007) Mass-dependent and -independent fractionation of Hg isotopes by photoreduction in aquatic systems. *Science* **318**, 417–420.

Biester H., Bindler R., Martinez-Cortizas A. and Engstrom D. R. (2007) Modeling the past atmospheric deposition of mercury using natural archives. *Environ. Sci. Technol.* **41**, 4851–4860.

Blum J. D. and Bergquist B. A. (2007) Reporting of variations in the natural isotopic composition of mercury. *Anal. Bioanal. Chem.* **388**, 353–359.

Blum J. D., Popp B. N., Drazen J. C., Anela Choy C. and Johnson M. W. (2013) Methylmercury production below the mixed layer in the North Pacific Ocean. *Nat. Geosci.* **6**, 879–884.

Blum J. D., Sherman L. S. and Johnson M. W. (2014) Mercury isotopes in earth and environmental sciences. *Annu. Rev. Earth Planet. Sci.* **42**, 249–269.

Bowman K. L., Hammerschmidt C. R., Lamborg C. H. and Swarr G. (2015) Mercury in the North Atlantic Ocean: the U.S. GEOTRACES zonal and meridional sections. *Deep-Sea Res. PT. II* **116**, 251–261.

Buchachenko A. L. (2001) Magnetic isotope effect: nuclear spin control of chemical reactions. *J. Phys. Chem. A* **105**, 9995–10011.

Buchachenko A. L. (2009) Mercury isotope effects in the environmental chemistry and biochemistry of mercury-containing compounds. *Russ. Chem. Rev.* **78**, 319.

Cai H. and Chen J. (2015) Mass-independent fractionation of even mercury isotopes. *Sc. Bull.* **61**, 116–124.

Chen J., Hintelmann H., Feng X. and Dimock B. (2012) Unusual fractionation of both odd and even mercury isotopes in precipitation from Peterborough, ON. *Canada. Geochim. Cosmochim. Acta* **90**, 33–46.

Demers J. D., Blum J. D. and Zak D. R. (2013) Mercury isotopes in a forested ecosystem: implications for air-surface exchange dynamics and the global mercury cycle. *Global Biogeochem. Cycles* **27**, 222–238.

Demers J. D., Sherman L. S., Blum J. D., Marsik F. J. and Dvonch J. T. (2015) Coupling atmospheric mercury isotope ratios and meteorology to identify sources of mercury impacting a coastal urban-industrial region near Pensacola, Florida, USA. *Global Biogeochem. Cycles* **29**, 1689–1705.

Donovan P. M., Blum J. D., Yee D., Gehrke G. E. and Singer M. B. (2013) An isotopic record of mercury in San Francisco Bay sediment. *Chem. Geol.* **349–350**, 87–98.

Engstrom D. R., Fitzgerald W. F., Cooke C. A., Lamborg C. H., Drevnick P. E., Swain E. B., Balogh S. J. and Balcom P. H. (2014) Atmospheric Hg emissions from preindustrial gold and silver extraction in the Americas: a reevaluation from lake-sediment archives. *Environ. Sci. Technol.* **48**, 6533–6543.

Enrico M., Roux G. L., Marusczak N., Heimbürger L.-E., Claustres A., Fu X., Sun R. and Sonke J. E. (2016) Atmospheric mercury transfer to peat bogs dominated by gaseous elemental mercury dry deposition. *Environ. Sci. Technol.* **50**, 2405–2412.

Estrade N., Carignan J., Sonke J. E. and Donard O. F. X. (2009) Mercury isotope fractionation during liquid-vapor evaporation experiments. *Geochim. Cosmochim. Acta* **73**, 2693–2711.

Foucher D., Ogrinc N. and Hintelmann H. (2009) Tracing mercury contamination from the Idrija Mining Region (Slovenia) to the gulf of trieste using Hg isotope ratio measurements. *Environ. Sci. Technol.* **43**, 33–39.

Fu X., Marusczak N., Wang X., Gheusi F. and Sonke J. E. (2016) Isotopic composition of gaseous elemental mercury in the free troposphere of the Pic du Midi observatory. *France. Environ. Sci. Technol.* **50**, 5641–5650.

Gehrke G. E., Blum J. D. and Meyers P. A. (2009) The geochemical behavior and isotopic composition of Hg in a mid-Pleistocene western Mediterranean sapropel. *Geochim. Cosmochim. Acta* **73**, 1651–1665.

Ghosh S., Schauble E. A., Lacrampe Couloume G., Blum J. D. and Bergquist B. A. (2013) Estimation of nuclear volume dependent fractionation of mercury isotopes in equilibrium liquid–vapor evaporation experiments. *Chem. Geol.* **336**, 5–12.

Gratz L. E., Keeler G. J., Blum J. D. and Sherman L. S. (2010) Isotopic composition and fractionation of mercury in great lakes precipitation and ambient air. *Environ. Sci. Technol.* **44**, 7764–7770.

Gray J. E., Pribil M. J. and Higueras P. L. (2013) Mercury isotope fractionation during ore retorting in the Almadén mining district, Spain. *Chem. Geol.* **357**, 150–157.

Hararuk O., Obrist D. and Luo Y. (2013) Modelling the sensitivity of soil mercury storage to climate-induced changes in soil carbon pools. *Biogeosciences* **10**, 2393–2407.

Hintelmann H. (2012) Use of Stable Isotopes in Mercury Research. In *Mercury in the Environment: Pattern and Process* (ed. M. Bank). University Press Scholarship Online.

Hoefs J. (2015) *Stable Isotope Geochemistry*, seventh ed. Springer International Publishing, Switzerland.

Holmes C. D., Jacob D. J., Corbitt E. S., Mao J., Yang X., Talbot R. and Slemr F. (2010) Global atmospheric model for mercury including oxidation by bromine atoms. *Atmos. Chem. Phys.* **10**, 12037–12057.

Horowitz H. M., Jacob D. J., Amos H. M., Streets D. G. and Sunderland E. M. (2014) Historical mercury releases from commercial products: global environmental implications. *Environ. Sci. Technol.* **48**, 10242–10250.

Horowitz H. M., Jacob D. J., Zhang Y., Dibble T. S., Slemr F., Amos H. M., Schmidt J. A., Corbitt E. S., Marais E. A. and Sunderland E. M. (2017) A new mechanism for atmospheric mercury redox chemistry: implications for the global mercury budget. *Atmos. Chem. Phys.* **17**, 6353–6371.

Huang J. and Gustin M. S. (2015) Use of passive sampling methods and models to understand sources of mercury deposition to high elevation sites in the Western United States. *Environ. Sci. Technol.* **49**, 432–441.

Jiskra M., Wiederhold J. G., Bourdon B. and Kretzschmar R. (2012) Solution speciation controls mercury isotope fractionation of Hg(II) sorption to goethite. *Environ. Sci. Technol.* **46**, 6654–6662.

Jiskra M., Wiederhold J. G., Skyllberg U., Kronberg R.-M., Hajdas I. and Kretzschmar R. (2015) Mercury deposition and Re-emission pathways in boreal forest soils investigated with Hg isotope signatures. *Environ. Sci. Technol.* **49**, 7188–7196.

Jiskra M., Sonke J. E., Obrist D., Bieser J., Ebinghaus R., Myhre C. L., Pfaffhuber K. A., Wängberg I., Kyllönen K., Worthy D., Martin L. G., Labuschagne C., Mkololo T., Ramonet M., Magand O. and Dommergue A. (2018) A vegetation control on seasonal variations in global atmospheric mercury concentrations. *Nat. Geosci.* **11**, 244–250.

Keeler G., Glinsorn G. and Pirrone N. (1995) Particulate mercury in the atmosphere: its significance, transport, transformation and sources. *Water Air Soil Pollut.* **80**, 159–168.

Kritee K., Blum J. D., Johnson M. W., Bergquist B. A. and Barkay T. (2007) Mercury stable isotope fractionation during reduction of Hg(II) to Hg(0) by mercury resistant microorganisms. *Environ. Sci. Technol.* **41**, 1889–1895.

Kritee K., Blum J. D. and Barkay T. (2008) Mercury stable isotope fractionation during reduction of Hg(II) by different microbial pathways. *Environ. Sci. Technol.* **42**, 9171–9177.

Kritee K., Motta L. C., Blum J. D., Tsui M. T.-K. and Reinfelder J. R. (2018) Photomicrobial visible light-induced magnetic mass independent fractionation of mercury in a marine microalga. *ACS Earth Space Chem.* **2**, 432–440.

Laffont L., Sonke J. E., Maurice L., Monrroy S. L., Chincheros J., Amouroux D. and Behra P. (2011) Hg speciation and stable isotope signatures in human hair as a tracer for dietary and occupational exposure to mercury. *Environ. Sci. Technol.* **45**, 9910–9916.

Lamborg C. H., Fitzgerald W. F., Damman A. W. H., Benoit J. M., Balcom P. H. and Engstrom D. R. (2002) Modern and historic atmospheric mercury fluxes in both hemispheres: global and regional mercury cycling implications. *Global Biogeochem. Cycles* **16**, 1104.

Lamborg C. H., Hammerschmidt C. R., Bowman K. L., Swarr G. J., Munson K. M., Ohnemus D. C., Lam P. J., Heimburger L.-E., Rijkenberg M. J. A. and Saito M. A. (2014) A global ocean inventory of anthropogenic mercury based on water column measurements. *Nature* **512**, 65–68.

Li M., Sherman L. S., Blum J. D., Grandjean P., Mikkelsen B., Weihe P., Sunderland E. M. and Shine J. P. (2014) Assessing Sources of Human Methylmercury Exposure Using Stable Mercury Isotopes. *Environ. Sci. Technol.* **48**, 8800–8806.

Lindberg S. E. and Stratton W. J. (1998) Atmospheric mercury speciation: concentrations and behavior of reactive gaseous mercury in ambient air. *Environ. Sci. Technol.* **32**, 49–57.

Lindberg S., Bullock R., Ebinghaus R., Engstrom D., Feng X., Fitzgerald W., Pirrone N., Prestbo E. and Seigneur C. (2007) A synthesis of progress and uncertainties in attributing the sources of mercury in deposition. *Ambio* **36**, 19–33.

Manceau A., Wang J., Rovezzi M., Glatzel P. and Feng X. (2018) Biogenesis of mercury-sulfur nanoparticles in plant leaves from atmospheric gaseous mercury. *Environ. Sci. Technol.* **52**, 3935–3948.

Mason R. P., Fitzgerald W. F. and Morel F. M. M. (1994) The biogeochemical cycling of element mercury – anthropogenic influences. *Geochim. Cosmochim. Acta* **58**, 3191–3198.

Mason R. P., Choi A. L., Fitzgerald W. F., Hammerschmidt C. R., Lamborg C. H., Soerensen A. L. and Sunderland E. M. (2012) Mercury biogeochemical cycling in the ocean and policy implications. *Environ. Res.* **119**, 101–117.

Mead C., Lyons J. R., Johnson T. M. and Anbar A. D. (2013) Unique Hg stable isotope signatures of compact fluorescent lamp-sourced Hg. *Environ. Sci. Technol.* **47**, 2542–2547.

Mil-Homens M., Blum J., Canário J., Caetano M., Costa A. M., Lebreiro S. M., Trancoso M., Richter T., de Stigter H., Johnson M., Branco V., Cesário R., Mouro F., Mateus M., Boer W. and Melo Z. (2013) Tracing anthropogenic Hg and Pb input using stable Hg and Pb isotope ratios in sediments of the central Portuguese Margin. *Chem. Geol.* **336**, 62–71.

Nriagu J. O. (1979) Production and uses of mercury. In *Biogeochemistry of Mercury in the Environment* (ed. J. O. Nriagu). Elsevier, Amsterdam, pp. 23–39.

Obrist D., Pokharel A. K. and Moore C. (2014) Vertical profile measurements of soil air suggest immobilization of gaseous elemental mercury in mineral soil. *Environ. Sci. Technol.* **48**, 2242–2252.

Obrist D., Agnan Y., Jiskra M., Olson C. L., Colegrove D. P., Hueber J., Moore C. W., Sonke J. E. and Helmig D. (2017) Tundra uptake of atmospheric elemental mercury drives Arctic mercury pollution. *Nature* **547**, 201–204.

Perrot V., Pastukhov M. V., Epov V. N., Husted S., Donard O. F. X. and Amouroux D. (2012) Higher Mass-Independent Isotope Fractionation of Methylmercury in the Pelagic Food Web of Lake Baikal (Russia). *Environ. Sci. Technol.* **46**, 5902–5911.

Pongprueksa P., Lin C. J., Lindberg S. E., Jang C., Braverman T., Bullock O. R., Ho T. C. and Chu H. W. (2008) Scientific uncertainties in atmospheric mercury models III: boundary and initial conditions, model grid resolution, and Hg(II) reduction mechanism. *Atmos. Environ.* **42**, 1828–1845.

Pyle D. M. and Mather T. A. (2003) The importance of volcanic emissions for the global atmospheric mercury cycle. *Atmos. Environ.* **37**, 5115–5124.

Rose C. H., Ghosh S., Blum J. D. and Bergquist B. A. (2015) Effects of ultraviolet radiation on mercury isotope fractionation during photo-reduction for inorganic and organic mercury species. *Chem. Geol.* **405**, 102–111.

Ruaibarz A., Bolea F. E., Maage A., Frantzen S., Valdersnes S. and Vanhaecke F. (2016) Assessment of Hg pollution released from a WWII submarine wreck (U-864) by Hg isotopic analysis of sediments and Cancer pagurus tissues. *Environ. Sci. Technol.* **50**, 10361–10369.

Schauble E. A. (2007) Role of nuclear volume in driving equilibrium stable isotope fractionation of mercury, thallium, and other very heavy elements. *Geochim. Cosmochim. Acta* **71**, 2170–2189.

Selin N. E., Jacob D. J., Yantosca R. M., Strode S., Jaeglé L. and Sunderland E. M. (2008) Global 3-D land-ocean-atmosphere model for mercury: present-day versus preindustrial cycles and anthropogenic enrichment factors for deposition. *Global Biogeochem. Cycles* **22**, GB2011.

Senn D. B., Chesney E. J., Blum J. D., Bank M. S., Maage A. and Shine J. P. (2010) Stable Isotope (N, C, Hg) Study of Methylmercury Sources and Trophic Transfer in the Northern Gulf of Mexico. *Environ. Sci. Technol.* **44**, 1630–1637.

Sherman L. S., Blum J. D., Johnson K. P., Keeler G. J., Barres J. A. and Douglas T. A. (2010) Mass-independent fractionation of mercury isotopes in Arctic snow driven by sunlight. *Nat. Geosci.* **3**, 173–177.

Sherman L. S., Blum J. D., Keeler G. J., Demers J. D. and Dvonch J. T. (2012) Investigation of local mercury deposition from a coal-fired power plant using mercury isotopes. *Environ. Sci. Technol.* **46**, 382–390.

Sherman L. S., Blum J. D., Dvonch J. T., Gratz L. E. and Landis M. S. (2015) The use of Pb, Sr, and Hg isotopes in Great Lakes precipitation as a tool for pollution source attribution. *Sci. Total Environ.* **502**, 362–374.

Skyllberg U., Bloom P. R., Qian J., Lin C.-M. and Bleam W. F. (2006) Complexation of mercury(II) in soil organic matter: EXAFS evidence for linear two-coordination with reduced sulfur groups. *Environ. Sci. Technol.* **40**, 4174–4180.

Sonke J. E. (2011) A global model of mass independent mercury stable isotope fractionation. *Geochim. Cosmochim. Acta* **75**, 4577–4590.

Sonke J. E. and Blum J. D. (2013) Advances in mercury stable isotope biogeochemistry. *Chem. Geol.* **336**, 1–4.

Sonke J. E., Zambardi T. and Toutain J.-P. (2008) Indirect gold trap-MC-ICP-MS coupling for Hg stable isotope analysis using a syringe injection interface. *J. Anal. At. Spectrom.* **23**, 569–573.

Streets D. G., Devane M. K., Lu Z., Bond T. C., Sunderland E. M. and Jacob D. J. (2011) All-time releases of mercury to the atmosphere from human activities. *Environ. Sci. Technol.* **45**, 10485–10491.

Štrok M., Baya P. A. and Hintelmann H. (2015) The mercury isotope composition of Arctic coastal seawater. *C. R. Geosci.* **347**, 368–376.

Štrok M., Hintelmann H. and Dimock B. (2014) Development of pre-concentration procedure for the determination of Hg isotope ratios in seawater samples. *Anal. Chim. Acta* **851**, 57–63.

Sun G., Sommar J., Feng X., Lin C.-J., Ge M., Wang W., Yin R., Fu X. and Shang L. (2016a) Mass-dependent and -independent fractionation of mercury isotope during gas-phase oxidation of elemental mercury vapor by atomic Cl and Br. *Environ. Sci. Technol.* **50**, 9232–9241.

Sun R., Streets D. G., Horowitz H. M., Amos H. M., Liu G., Perrot V., Toutain J.-P., Hintelmann H., Sunderland E. M. and Sonke J. E. (2016b) Historical (1850–2010) mercury stable isotope inventory from anthropogenic sources to the atmosphere. *Elem. Sci. Anth.* **4**, 000091.

Sunderland E. M. and Mason R. P. (2007) Human impacts on open ocean mercury concentrations. *Global Biogeochem. Cycles* **21**, GB4022.

Wang Z., Chen J., Feng X., Hintelmann H., Yuan S., Cai H., Huang Q., Wang S. and Wang F. (2015) Mass-dependent and mass-independent fractionation of mercury isotopes in precipitation from Guiyang, SW China. *C. R. Geosci.* **347**, 358–367.

Wang X., Luo J., Yin R., Yuan W., Lin C.-J., Sommar J., Feng X., Wang H. and Lin C. (2017) Using mercury isotopes to understand mercury accumulation in the montane forest floor of the eastern Tibetan plateau. *Environ. Sci. Technol.* **51**, 801–809.

Wiederhold J. G. (2015) Metal stable isotope signatures as tracers in environmental geochemistry. *Environ. Sci. Technol.* **49**, 2606–2624.

Wiederhold J. G., Cramer C. J., Daniel K., Infante I., Bourdon B. and Kretzschmar R. (2010) Equilibrium mercury isotope fractionation between dissolved Hg(II) species and thiol-bound Hg. *Environ. Sci. Technol.* **44**, 4191–4197.

Wiederhold J. G., Skyllberg U., Drott A., Jiskra M., Jonsson S., Björn E., Bourdon B. and Kretzschmar R. (2015) Mercury isotope signatures in contaminated sediments as a tracer for local industrial pollution sources. *Environ. Sci. Technol.* **49**, 177–185.

Xu H., Sonke J. E., Guinot B., Fu X., Sun R., Lanzanova A., Candaudap F., Shen Z. and Cao J. (2017) Seasonal and annual variations in atmospheric Hg and Pb isotopes in Xi'an. *China. Environ. Sci. Technol.* **51**, 3759–3766.

Yang L. and Sturgeon R. (2009) Isotopic fractionation of mercury induced by reduction and ethylation. *Anal. Bioanal. Chem.* **393**, 377–385.

Yin R., Feng X. and Meng B. (2013) Stable mercury isotope variation in rice plants (Oryza sativa L.) from the Wanshan mercury mining district, SW China. *Environ. Sci. Technol.* **47**, 2238–2245.

Yin R., Feng X., Li X., Yu B. and Du B. (2014) Trends and advances in mercury stable isotopes as a geochemical tracer. *Trends Environ. Anal. Chem.* **2**, 1–10.

Yin R., Feng X., Chen B., Zhang J., Wang W. and Li X. (2015) Identifying the sources and processes of mercury in subtropical estuarine and ocean sediments using Hg isotopic composition. *Environ. Sci. Technol.* **49**, 1347–1355.

Yu B., Fu X., Yin R., Zhang H., Wang X., Lin C.-J., Wu C., Zhang Y., He N., Fu P., Wang Z., Shang L., Sommar J., Sonke J. E., Maurice L., Guinot B. and Feng X. (2016) Isotopic composition of atmospheric mercury in China: new evidence for sources and transformation processes in air and in vegetation. *Environ. Sci. Technol.* **50**, 9262–9269.

Yuan S., Zhang Y., Chen J., Kang S., Zhang J., Feng X., Cai H., Wang Z., Wang Z. and Huang Q. (2015) Large variation of mercury isotope composition during a single precipitation event at Lhasa City, Tibetan Plateau, China. *Proc. Earth Planet. Sci.* **13**, 282–286.

Yuan S., Chen J., Cai H., Yuan W., Wang Z., Huang Q., Liu Y. and Wu X. (2018) Sequential samples reveal significant variation of mercury isotope ratios during single rainfall events. *Sci. Total Environ.* **624**, 133–144.

Zambardi T., Sonke J. E., Toutain J. P., Sortino F. and Shinohara H. (2009) Mercury emissions and stable isotopic compositions at Vulcano Island (Italy). *Earth Planet. Sci. Lett.* **277**, 236–243.

Zhang H., Yin R., Feng X., Sommar J., Anderson C. W. N., Sapkota A., Fu X. and Larssen T. (2013) Atmospheric mercury inputs in montane soils increase with elevation: evidence from mercury isotope signatures. *Sci. Rep.* **3**, 3322.

Zhang Y., Jaeglé L., Thompson L. and Streets D. G. (2014) Six centuries of changing oceanic mercury. *Global Biogeochem. Cycles* **28**, 1251–1261.

Zhang Y., Jacob D. J., Dutkiewicz S., Amos H. M., Long M. S. and Sunderland E. M. (2015) Biogeochemical drivers of the fate of riverine mercury discharged to the global and Arctic oceans. *Global Biogeochem. Cycles* **29**, 854–864.

Zheng W., Foucher D. and Hintelmann H. (2007) Mercury isotope fractionation during volatilization of Hg(0) from solution into the gas phase. *J. Anal. At. Spectrom.* **22**, 1097–1104.

Zheng W. and Hintelmann H. (2009) Mercury isotope fractionation during photoreduction in natural water is controlled by its Hg/DOC ratio. *Geochim. Cosmochim. Acta* **73**, 6704–6715.

Zheng W. and Hintelmann H. (2010a) Isotope fractionation of mercury during its photochemical reduction by low-molecu-lar-weight organic compounds. *J. Phys. Chem. A* **114**, 4246–4253.

Zheng W. and Hintelmann H. (2010b) Nuclear field shift effect in isotope fractionation of mercury during abiotic reduction in the absence of light. *J. Phys. Chem. A* **114**, 4238–4245.

Zheng W., Obrist D., Weis D. and Bergquist B. A. (2016) Mercury isotope compositions across North American forests. *Global Biogeochem. Cycles* **30**. https://doi.org/10.1002/2015GB005323.

Associate editor: Jan G. Wiederhold